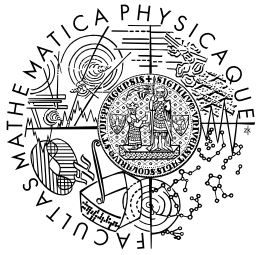

FACULTY
OF MATHEMATICS
AND PHYSICS
Charles University

MASTER THESIS

Bc. Yelyzaveta Pulnova

Particle acceleration and magnetic-field amplification in the termination shocks of AGN jets

Institute of Theoretical Physics

Supervisor of the master thesis: Anabella Teresa Araudo, Ph.D.
Study programme: Physics
Study branch: Theoretical Physics

Prague 2021

I declare that I carried out this master thesis independently, and only with the cited sources, literature and other professional sources. It has not been used to obtain another or the same degree.

I understand that my work relates to the rights and obligations under the Act No. 121/2000 Sb., the Copyright Act, as amended, in particular the fact that the Charles University has the right to conclude a license agreement on the use of this work as a school work pursuant to Section 60 subsection 1 of the Copyright Act.

In ..... date ....

Author's signature

My sincere gratitude belongs to my supervisor Dr. Anabella Teresa Araudo, for her valuable guidance, support, and sharing her extensive knowledge with me. I very much thank Dr. Ana Laura Müller for the insightful discussions. I further thank prof. Sergei Bulanov for the help with section 1.3.3. I would like to thank my professors from the Institute of Theoretical physics for the priceless experience and all the knowledge I had the honor to gain at ITF.

I am deeply grateful to my family for their love and everlasting support.

Title: Particle acceleration and magnetic-field amplification in the termination shocks of AGN jets

Author: Bc. Yelyzaveta Pulnova

Institute: Institute of Theoretical Physics

Supervisor: Anabella Teresa Araudo, Ph.D., ELI Beamlines - International Laser Research Centre, 25241 Dolní Břežany, Czech Republic;
Laboratoire Univers et Particules de Montpellier (LUPM) Université Montpellier, CNRS, France;
Astronomical Institute, Czech Academy of Sciences.

Abstract: The origin of Ultra-High-Energy Cosmic Rays (UHECRs) is still an open question in Astrophysics. The scope of this thesis is the study of the termination shocks in the jets of radiogalaxies 3C 105, 3C 227, and 3C 445 as cosmic rays accelerators. We assume the diffusive shock acceleration (DSA) and that the maximum energy is determined by the escape of CRs downstream of the shock due to the magnetization. We find maximum achievable energy of non-thermal electrons and protons, which appeared to be only $\sim$ TeV. Therefore the reverse shocks of AGNs' jets are not the sources of UHECRs. We also implement the model, where the scattering centers for the DSA emerge from the non-resonant hybrid instabilities in plasma. We take into account the results from the numerical simulations and observations that indicate the amplification of the magnetic field by orders of magnitude, and we obtain results that qualitatively fit the simulation outcome.

Keywords: ultra-high-energy cosmic rays, termination shock wave, diffusive shock acceleration,non-resonant hybrid instabilities

Contents

Preface

Cosmic rays (CR) are charged particles of extraterrestrial origin. Most of them are originated on the Sun with typical energies below 10 GeV; others are believed to come from both inside ($E \leq 3\,\mathrm{EeV}$) and outside ($E > 3\,\mathrm{EeV}$) of the Milky Way [Gaisser et al., 2016]. In particular, most of the Galactic CR are accelerated in supernova remannats. Ultra-high Energy Cosmic Rays (UHECR) are particles with energy $E > 10^{18}\,\mathrm{eV}$. The physical process that could drive such an efficient acceleration mechanism is still not fully understood.

From detections of UHECR, we know that their distribution in the sky is anisotropic [Abbasi et al., 2014]. Nevertheless, the angular size of the source regions is rather large and can not be unambiguously associated with particular astrophysical objects. It was demonstrated that the directions of the arriving UHECR are correlated with the locations of Active Galactic Nuclei (AGN) and Starburst galaxies [Aab et al., 2017], [Matthews et al., 2018].

In this thesis we study AGNs. Among all possible acceleration processes at different parts of AGN, such as acceleration in the ergosphere of a black hole or on the internal shocks of the jet, we examine in our research the diffusive shock acceleration (DSA) on the shock in the termination region of the AGN's jets. We apply a model developed by [Araudo et al., 2016] and [Bell et al., 2018] to three particular sources where high spatial resolution data are available in the literature.

The thesis is organized as follows: In chapter 1, we introduce theoretical aspects of the diffusive shock acceleration (DSA). In chapter 2, we describe the chosen set of radiogalaxies and examine their key parameters. We discuss possible processes that could limit maximum energy of electrons and estimate the corresponding values of protons and electrons maximum energy. In chapter 3, we introduce the non-resonant hybrid instabilities (NRH), provide arguments on magnetic field amplification and apply the requirements for DSA together with NRH instabilities to be consistent with evidence available from observations and simulations. In addition, we support the assumption of the perpendicular configuration of the magnetic field in the hotspots through a critical magnetic field.

We work in cgs units.

Chapter 1

Theoretical overview

Ultra-high Energy Cosmic Rays are charged particles. For both ions and electrons, the detected energy spectra are power-law of a similar slope $N(E) \sim E^{-s}$. In the ions spectrum, there are two breaks where the spectral index s changes (see fig. 1.1. After starting at $s \sim 2.7$ for the lower energies, it steepens at so-called the 'knee' of the spectrum ($E \sim 3\,\mathrm{PeV}$) to the value $s \sim 3.1$. This is believed to be the result of a leakage of the particles from the galactic confinement, as the cutoff of light elements is observed at the same energy [Hörandel, 2007]. At even higher energies, the spectrum flattens again at the 'ankle' ($E \sim 10\,\mathrm{EeV}$) and cuts off around $10^{20}\,\mathrm{EeV}$. The theory that justifies an upper boundary for the CR energy is the so-called Greisen–Zatsepin–Kuzmin (GZK) limit. We expect the energy spectrum of CR to have an upper limit around $5 \cdot 10^{19}$ eV. Above this energy, CR would interact with cosmic microwave background photons and start losing energy, producing pions through photodisintegration [Zatsepin and Kuz'min, 1966]. However, if particle acceleration occurs close to Earth (inside of a GZK horizon$\sim$ 50 Mpc [Burde, 2021]) the interactions may not have enough time to reduce CR energy.

In context of the possible candidates of UHECR sources Hillas [1984] derived a simple requirement on a combination of source's size L and magnetic field intensity B that is depicted in fig. 1.2. The parameters of the source should lie above the line on fig. 1.2 to become a candidate for the acceleration of a given particle up to the required energy. The Hillas energy is an upper limit for the achievable energy in a given source. From fig. 1.2 we see that active galactic nuclei fulfill the Hillas requirement, and thus we proceed further in the study of AGN as possible UHECR accelerators.

As we will see, the Hillas energy is not reachable mainly due to the fact that CR escape earlier than achieve the maximum energy.

1.1 The anatomy of AGN

The term 'active' in the name of AGN points to the characteristic feature that distinguishes AGN from the regular galaxies - the presence of an active supermassive black hole in its center. The typical AGN consists of a supermassive black hole, an accretion disc, which provides matter for the formation of two jets along the rotation axis. AGNs that are loud in radio waveband are called radiogalaxies. They are classified into two groups according to the Fanaroff–Riley (FR) scheme

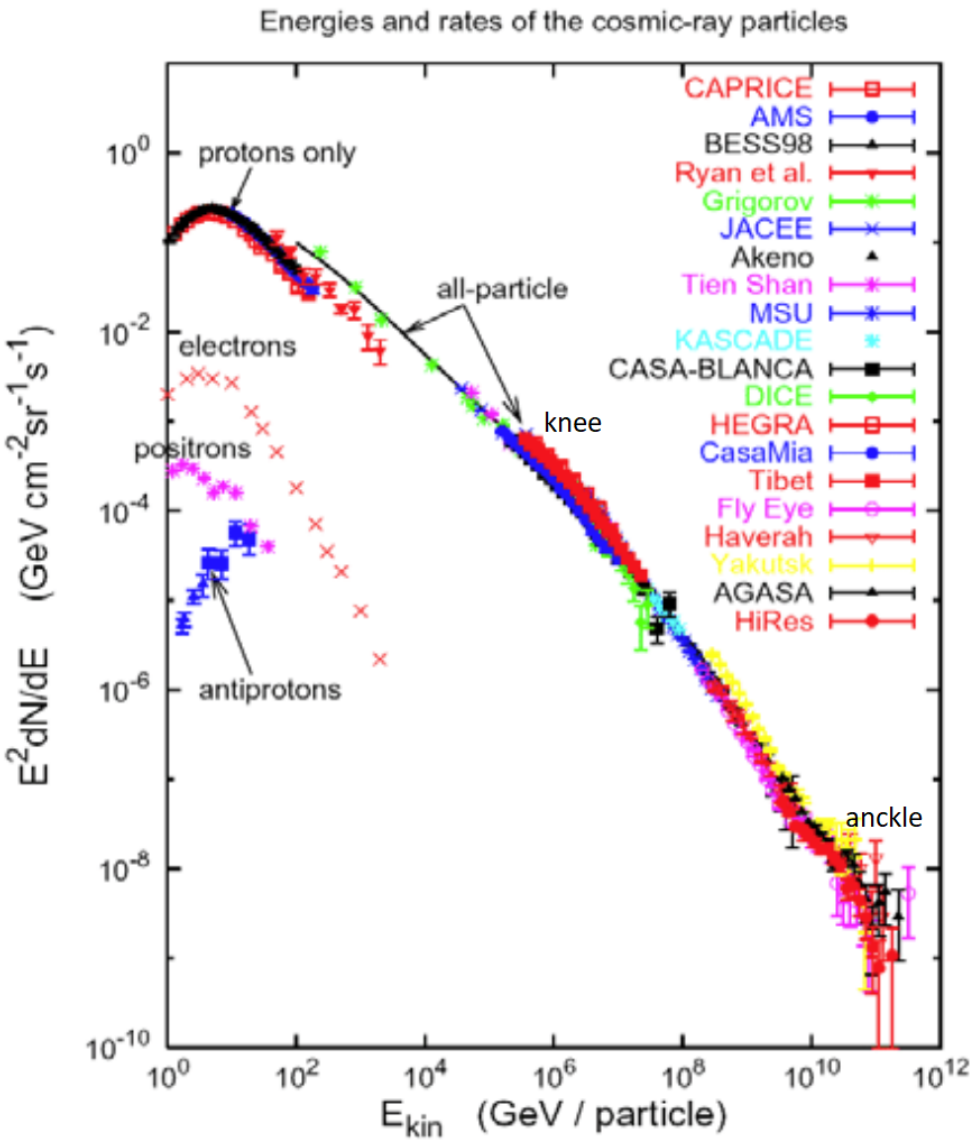

Figure 1.1: Energy spectra of cosmic rays with different atomic number. Credit: [Diehl, 2009].

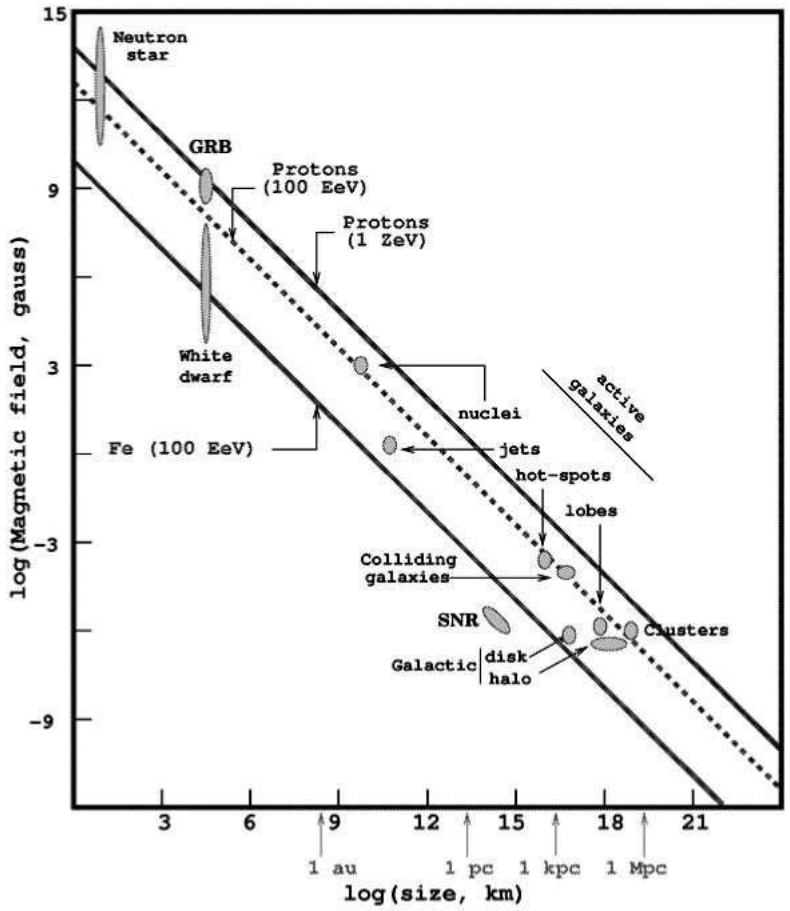

Figure 1.2: Hillas plot. Diagonal lines correspond to the fixed maximum energy of a CR reachable for a given size and magnetic field in the source. Some chosen sources are depicted on the plot. Those which lies on or above a given line have a potential to accelerate CR to a corresponding energy. The upper line states protons of energy $E_{\rm p} \sim$ ZeV, the dashed one $E_p \sim 100\,$EeV, the lower line the iron nuclei $E_{\rm Fe} \sim 100\,$EeV. Credit: [Gelmini, 2009].

([Fanaroff and Riley, 1974]). The main difference between the two groups is the relative location of the significant emission in the radiogalaxy (see fig. 1.3). In case when the energy loss is small near the core and along with the jets (FR II-type), the main emission is localized at the jets' termination region, that is called a hotspot. In this thesis, we study particle acceleration and magnetic field amplification in the hotspots of FR II radiogalaxies' jets.

We study the termination regions of the jets, which typically have a double shock structure (see fig. 1.4) separated by a contact discontinuity [Smith et al., 1985] - the surface of pressure equilibrium between the matter of the jet and of the intergalactic medium (IGM) flows. The shock between the plasma of the jet and the IGM is called a bow shock (BS). The shock that separates a jet and a hotspot is called a reverse shock (RS). In this thesis, we concentrate on the acceleration process at the RS.

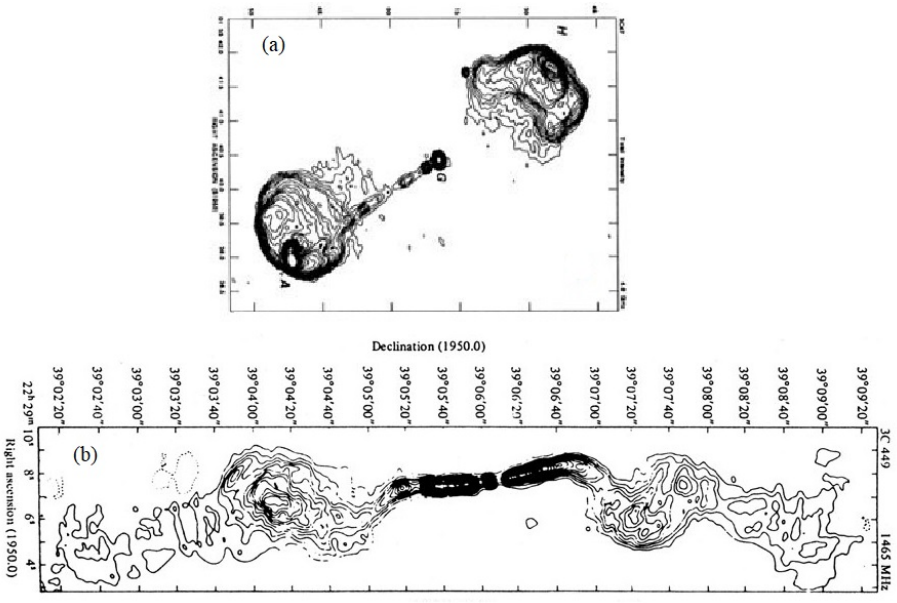

Figure 1.3: The sketch of the FR II-type radiogalaxy (a). Credit: [Bridle et al., 1994] and the FR I-type radiogalaxy (b). Credit: [Perley et al., 1979].

1.2 Shocks

A shock is a result of the supersonic propagation of matter. The quantities such as plasma density, temperature, and pressure change so rapidly that they can be treated as discontinuous at the wavefront.

We call the region in front of the shock **the upstream** (in the shock rest frame matter approaches the shock), and the region behind is correspondingly called **the downstream** (in the shock rest frame matter flows away from the shock). In particular, on fig. 1.4 for the bow shock, the upstream is IGM, and for the reverse shock, it is the jet medium.

The brightest emission in termination region of FR II radiogalaxies is detected downstream of the RS. The synchrotron emission is more effective in stronger magnetic field, as can be seen from the cooling time $t_{\text{synch}} = -E/\dot{E} \sim E^{-1}\, B^{-2}$ [Longair, 2010, p. 195], that is defined as a time by which a given particle will lose half of its initial energy. The plasma density downstream is compressed by a factor of $r \sim 3 - 4$, where r is a so-called compression ratio, that is defined from the mass conservation $\rho_1 u_1 = \rho_2 u_2$ on the shock front

$$r = \frac{u_1}{u_2} \equiv \frac{\rho_2}{\rho_1}. \tag{1.1}$$

Here ρ_1 and ρ_2 are densities upstream and downstream, respectively. The background plasma flow velocities are denoted by u_1 and u_2. The compression ratio r in terms of the heat capacity ratio γ and the Mach number M reads [Lifshitz and Landau, 1987]

$$\frac{u_1}{u_2} = \frac{\gamma + 1}{\gamma - 1 + 2/M^2}. \tag{1.2}$$

For the strong shock $M \gg 1$ it holds

$$r = \frac{\gamma - 1}{\gamma + 1}. \tag{1.3}$$

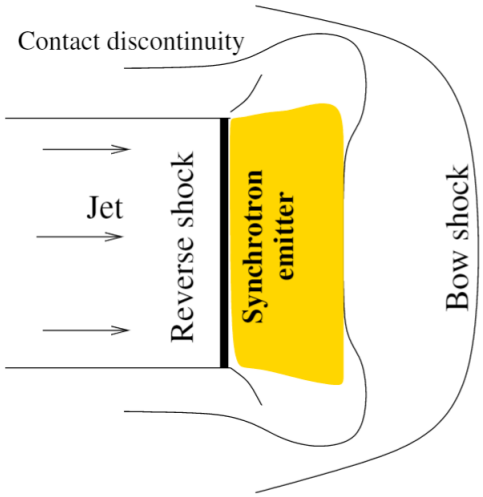

Figure 1.4: Jet termination region in the shock rest frame. The yellow region denotes the detected emission and is called the hotspot of the jet. We consider the acceleration on the reverse shock. Thus, the region to the left (jet plasma) we call upstream, and the synchrotron emitter region corresponds to downstream. Credit: [Araudo et al., 2016].

In astrophysical plasma, magnetic field lines can be treated as frozen in the matter. Thus, magnetic field intensity downstream is higher than upstream for about the same factor r. The synchrotron cooling is more efficient downstream as the cooling time is shorter. Nevertheless, as we will see in sec. 2.3.2, the magnetic field that is required for such synchrotron emission occurs to be significantly stronger than is expected due to the plasma compression $B = rB_{\rm jet}$. In chap. 3, we discuss the requirements to achieve such amplification.

In the following parts of the thesis, we will assume the so-called perpendicular configuration of the jet's reverse shock. That means that the magnetic field B lines are perpendicular to the shock normal. To justify this assumption, we introduce in this part the way of finding the reference frame, where the magnetic and electric fields E are perpendicular to the normal of the reverse shock of AGN jet.

1.2.1 On rest frames of the shock

The shock rest frame is preferable since CR acceleration takes place in the vicinity of the shock. Such a frame is not unique as any boost parallel to the shock surface is allowed. We will take advantage of the remaining freedom of a boost choice to simplify the field's configuration with respect to the shock front. From the special theory of relativity, we know that the components of the electric and magnetic fields are affected by the Lorentz boost. In the following part, we will quantify the changes for the magnetic field. Plasma is a highly conductive medium, so we expect no electric field in the upstream plasma rest frame. We assume the following initial configuration: the normal of the shock front $\mathbf{n}$ is aligned with an x-axis. Magnetic field is oriented so that $\mathbf{n} \cdot \mathbf{B} = B \cos\Phi$, where $\mathbf{B}$ is a magnetic field (see fig. 1.5). In any Lorentz boost, the parallel components of $\mathbf{E}$ and $\mathbf{B}$

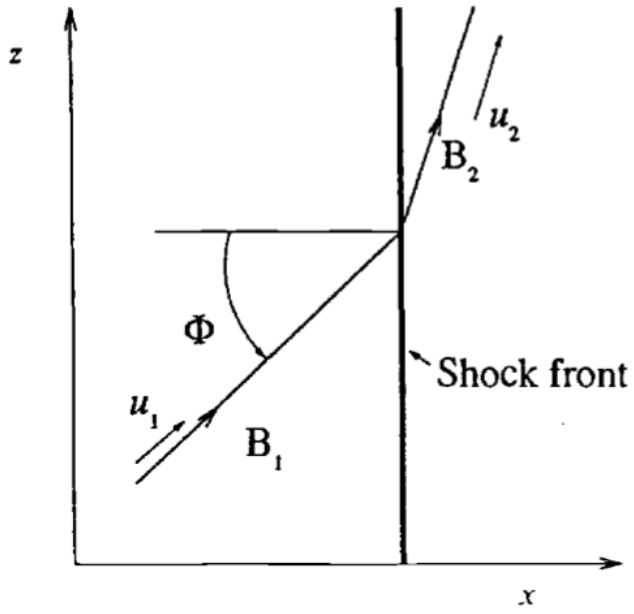

Figure 1.5: A subluminal shock front in the de Hoffmann/Teller reference frame. Shock appears to be stationary and there is no electric field in both upstream (appurtenant quantities carries subindeces '1') and downstream regions (subindeces '2'). Credit: [Kirk et al., 2006].

fields with respect to the boost velocity remain unchanged [Kirk et al., 2006]. To achieve the stationary shock, we need

$$v_{\rm boost} \cos\Phi = U, \tag{1.4}$$

where U is a shock velocity and $\mathbf{v}_{\rm boost}$ is a boost velocity. Geometrically such a boost corresponds to the boost with the propagation velocity of the intersection point between the magnetic field lines and the shock front. Such a frame is called de Hoffmann/Teller reference frame (see fig. 1.6).

The apparent velocity of the upstream plasma after the boosting 1.4 is then aligned with the magnetic field lines. The shock jump conditions imply that in the downstream region, the plasma flow is likewise parallel to the magnetic field.

The intersection point does not carry any information, and for shocks fast enough, it propagates faster than light $U/\cos\Phi > c$ (so-called superluminal shock), where c is a speed of light. In this case, we are not able to reach the stationary shock frame by the boost described above, but an additional boost will solve this problem.

From the expression, for the velocity of intersection point after being boosted

$$v_{\rm int} = \frac{v_{\rm boost} - U/\cos\Phi}{1 - v_{\rm boost} U/c^2 \cos\Phi}$$

it can be seen that for $v_{\rm boost} = c^2 \cos\Phi/U$ magnetic field lines become perpendicular to the shock normal. Nevertheless, shock is not at rest, so field lines approach the shock front with nonzero velocity. We can transform it away by boosting along with the shock normal. The resulting reference frame is referred as the **perpendicular shock frame** (fig. 1.6). As was mentioned above, such

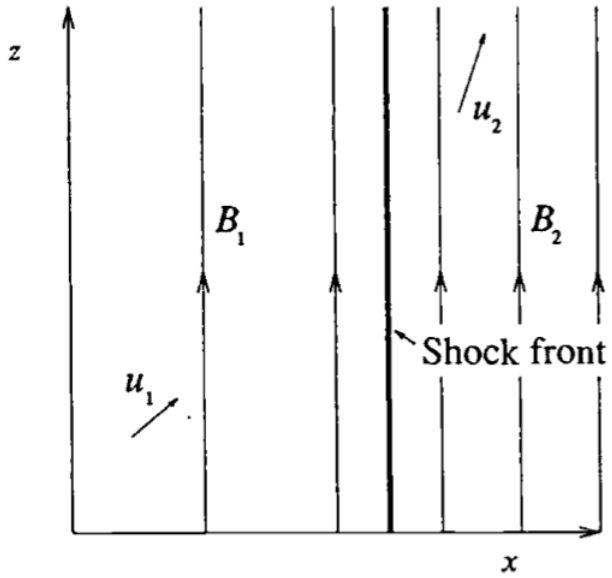

Figure 1.6: A superluminal shock in the perpendicular shock frame. Shock appears to be stationary. Vectors **E** and **B** are perpendicular and both lie in the plane of the shock Credit: [Kirk et al., 2006].

transformation will not affect the magnetic field, but an electric field will be generated. This indicates that the plasma is not aligned with the field lines anymore. So depending on the angle Φ between the unperturbed magnetic field B_0 and a shock normal in shock rest frame we distinguish:

- parallel shock ($\Phi = 0°$)
- perpendicular shock ($\Phi = 90°$)
- oblique shock

As follows from observations, in the laboratory rest frame, the propagation of the termination region of the jet in the IGM is non-relativistic. Nevertheless, due to the relativistic streaming velocity of the jet plasma (bulk Lorentz factor $\Gamma \geq 2$), an observer in the upstream of the RS sees the shock approaching at a relativistic speed. For this reason, the RS is considered to be relativistic.

Shocks in jets of AGNs are relativistic [Massaglia, 2003], which implies the perpendicular magnetic field in both upstream and downstream. Shock waves play a key role in the noteworthy acceleration process that we discuss in the following section.

1.3 Diffusive shock acceleration

The essence of diffusive shock acceleration is converting the macroscopic kinetic energy of magnetized plasma bulk into the kinetic energy of individual charged particles. DSA is a mechanism for the acceleration of the non-thermal[1] particles

[1]The vast majority of the particles in astrophysical plasma is following the Maxwell-Boltzmann velocity distribution. We call them thermal particles. Nevertheless, we observe

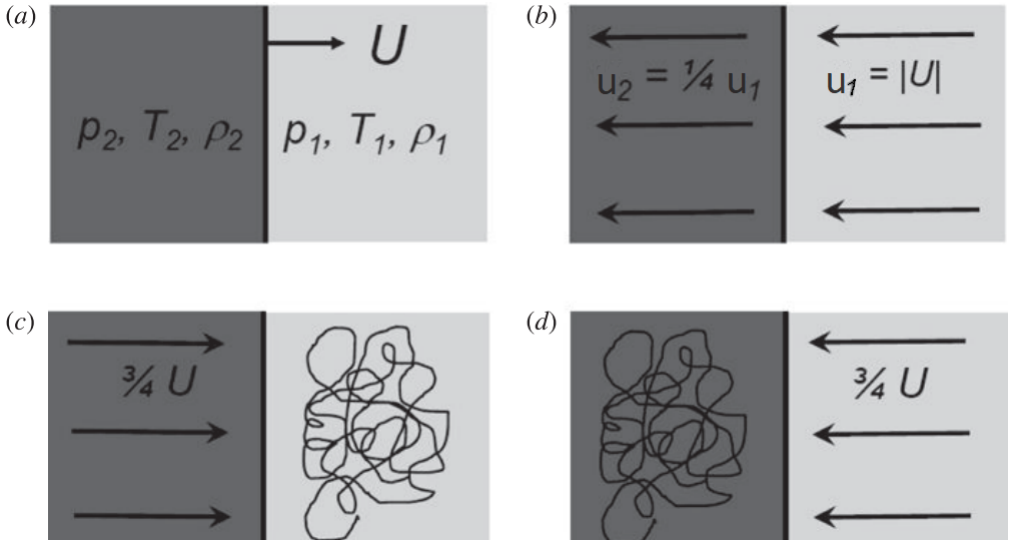

Figure 1.7: The propagation of the strong shock wave is depicted in various reference frames. Dark region corresponds to the downstream (with stationary density ρ_2, temperature T_2 and pressure p_2), light region - upstream (stationary ρ_1, T_1 and p_1). All relative velocities here are calculated under the assumption of non-relativistic shock velocity so that the heat capacity ratio $\gamma = 5/3$. (a) Laboratory rest frame. Shock propagates through the IGM with velocity U. (b) Shock rest frame. (c) Upstream rest frame. (d) Downstream rest frame. Credit: [Longair, 2010].

based on the multiple crossing of the shock front. To ensure these crossings, we require the presence of the scattering centers that would redirect particles back towards the shock. The role of such centers could play the waves naturally excited in the plasma due to the CR propagation. In section 3.1, we discuss these waves in more detail.

Diffusive shock acceleration is the 1$^{\text{st}}$ order Fermi acceleration [Krymskii, 1977], [Bell, 1978], [Blandford and Ostriker, 1978]. As we will see, the name is connected to the fact that the relative energy gain depends on the shock velocity as the *first* power.

1.3.1 Relative energy gain per shock crossing

First, let us introduce the idea in simple words. For better intuition, we present here fig. 1.7, where the shock's vicinity is depicted in different rest frames. Intuitively, the particle that undergoes an elastic head-on collision with magnetic field turbulence will gain some energy. This is, for instance, the case of the particle that flowing away from the shock meets the scattering center of the upstream. What, perhaps, could be more surprising is that the energy gain is the same in the situation of a head-on collision downstream (see fig. 1.7 (b)). This becomes more plausible once we consider that the particle is isotropized after some time in the given (upstream or downstream) region. Now, in the rest frame of the back-

more of them happen to achieve greater energies. These particles follow the power-law energy distribution, and we refer to them as non-thermal particles. In the case of AGN's jets, the fraction of such particles is around $\sim 1\%$.

ground plasma, the vicinity of the shock looks like in fig. 1.7 (c or d). As can be seen, the environment seems to be symmetric in both cases of the transition from the isotropic medium across the shock. Consequently, the energy gain will be the same, as we will illustrate just now.

For this purpose, we consider the single crossing of the shock front by a relativistic particle from upstream to downstream. The general form of the Lorentz transformation is

$$E = \gamma_V (E_0 + \mathbf{V} \cdot \mathbf{p}), \tag{1.5}$$

where $\mathbf{V}$ is a relative velocity between the initial and boosted reference frames, E_0 is initial energy of the particle, $\gamma_V = 1/\sqrt{1 - V^2/c^2}$ is the Lorentz factor corresponding to the boost with a velocity $\mathbf{V}$, and $\mathbf{p}$ is a momentum of the particle. We start in the upstream rest frame and boost into the downstream rest frame, so $V = |u_1 - u_2|$, where u_1 and u_2 are the background plasma velocities, defined according to fig. 1.7 (b). The particle crosses the shock at an angle θ. We choose the axis of $\theta = 0$ to be perpendicular to the shock front. Now eqn. 1.5 holds

$$E = \gamma_V (E_0 + Vp \cos\theta). \tag{1.6}$$

Assuming the non-relativistic shock $\gamma_V \sim 1$ and relativistic particle $p = E_0/c$ we can see that $\Delta E = E - E_0 = V/c \cos\theta$ and the relative energy change is then

$$\frac{\Delta E}{E} = \frac{V}{c} \cos\theta. \tag{1.7}$$

We are interested in the average energy change per single crossing, so we have to average over all possible values of θ.

We need to devise what is the probability of the particle to cross the shock within the angles θ to $\theta + d\theta$. As the distribution is isotropic, the 'angular probability density' is

$$p_{\text{direction}} = \frac{d\Omega}{\int d\Omega} = \frac{\sin\theta d\phi d\theta}{4\pi}. \tag{1.8}$$

Since we are interested only in θ, we eliminate the ϕ-dependence by integrating from 0 to 2π

$$p_1(\theta) = \frac{1}{2} \sin\theta d\theta. \tag{1.9}$$

Another factor that will have a significant role in whether or not the particle will cross the shock is the relative velocity with respect to the shock $v \cos\theta$. As $\theta = 0$ is a horizontal axis, we consider it to be in a range from 0 to $\pi/2$, multiplying the probability by 2 to account for the θ-axis symmetry. Normalization condition

$$\int_0^{\pi/2} p(\theta) d\theta = 2N \int_0^{\pi/2} p_1(\theta) v \cos\theta = 2Nv \int_0^{\pi/2} \frac{\sin\theta \cos\theta}{2} d\theta = 1 \tag{1.10}$$

gives a value of a normalization constant $N = 2/v$ and leaves us with the resulting probability of particle crossing the shock at a given angle

$$p(\theta) = 2 \sin\theta \cos\theta. \tag{1.11}$$

The average relative energy gain is then

$$\left\langle \frac{\Delta E}{E} \right\rangle = \int \frac{\Delta E}{E} p(\theta) d\theta = 2 \frac{V}{c} \int_0^{\pi/2} \sin\theta \cos^2\theta d\theta = \frac{2V}{3c}. \tag{1.12}$$

Let us emphasize once more the origin of the $\cos^2\theta$ in the eqn. 1.12. The first $\cos\theta$ comes from our specific choice of the boost in the direction of the shock normal. Another $\cos\theta$ in the eqn. 1.11 rises due to the geometry of the problem - orientation of the particle's velocity with respect to the shock normal.

Bearing in mind that $V = |u_1 - u_2|$ is an absolute value and comparing fig. 1.7 (c) and (d) we see, that the relative energy change would be the same in the backward shock crossing (having particle been in the medium long enough to become isotropic). We also see that $\langle \Delta E/E \rangle > 0$, so the relative energy gain for the whole round trip is

$$\left\langle \frac{\Delta E}{E} \right\rangle \Bigg|_{\text{round trip}} = \frac{4|u_1 - u_2|}{3c} = \frac{4V}{3c} \equiv \frac{U}{c}, \tag{1.13}$$

where U is a magnitude of the shock velocity in a laboratory rest frame.

1.3.2 The power-law energy distribution from DSA

From the diffusive shock acceleration, we will derive that the energy spectrum is power-law. We consider the particles of initial energy E_0 with a number density N_0. After the shock crossing, their energy is changed by some factor A. Some of the particles diffuse away from the shock, so the remaining number of particles after the transition is modified by the factor P. The corresponding energy and population number changes after the k cycles are

$$\langle E_1 \rangle = AE_0 \qquad \langle E_k \rangle = A^k E_0 \tag{1.14}$$

$$\langle N_1 \rangle = PN_0 \qquad \langle N_k \rangle = P^k N_0. \tag{1.15}$$

We then rewrite A in terms of relative energy change ΔE

$$A = \left\langle \frac{E}{E_0} \right\rangle = \left\langle \frac{E - E_0 + E_0}{E_0} \right\rangle = 1 + A \left\langle \frac{\Delta E}{E} \right\rangle. \tag{1.16}$$

The result for A is

$$A = \frac{1}{1 - \langle \Delta E/E \rangle} \approx 1 + \left\langle \frac{\Delta E}{E} \right\rangle. \tag{1.17}$$

Equating the k exponents from both equations 1.14 and 1.15 we get

$$\frac{\ln N}{\ln N_0} = \frac{\ln P}{\ln A} \implies \frac{N}{N_0} = \left(\frac{E}{E_0}\right)^{\frac{\ln P}{\ln A}}. \tag{1.18}$$

The differential energy spectrum is then

$$N(E)dE = \left(N_0 E_0^{-\frac{\ln P}{\ln A}} \ln P / \ln A \right) E^{\frac{\ln P}{\ln A} - 1} dE \propto E^{-s} dE, \tag{1.19}$$

where $s = 1 - \ln P / \ln A$ is often referred as the spectral index.

1.3.3 Number value of the power-law exponent for the non-relativistic plasma

Macroscopic treatment

We define the distribution function $f(\mathbf{x}, \mathbf{p}; t)$ for a single particle, which corresponds to the number density function of particles in 6-dimensional space of coordinates $\mathbf{x}$ and momenta $\mathbf{p}$ at a given time t. Our goal is a derivation of the distribution as an explicit momentum function. It will allow us to calculate the distribution for CR energy and compare it to the observational energy spectrum.

For the following derivation, we consider the shock rest frame as depicted in fig. 1.7 (b) with u_1 and u_2 oriented along the x-axis ($x = 0$ at the shock front). We assume plane shock lying in yz plane. In [Blandford and Eichler, 1987, eqn. (3.39)], the transport equation is derived for a stationary configuration and spatially constant diffusion coefficient ($D := \lambda c/3 \equiv D_{||}(p)$ in direction aligned with a shock normal). The izotropization, which occurs some time after the shock crossing, allows us to work with a distribution function averaged over the particle direction (θ, ϕ), leaving us with the convection-diffusion equation

$$-u(x)\frac{\partial f(x,p)}{\partial x} - \frac{\partial}{\partial x}\left(D\frac{\partial f(x,p)}{\partial x}\right) = \frac{1}{3}\frac{\partial u(x)}{\partial x}\,\mathrm{div}_p(pf(x,p)). \tag{1.20}$$

The velocity of the plasma $u(x)$ is constant everywhere except for the shock front, so the spatial derivation on the RHS is proportional to the Dirac delta function $\delta(x)$. Integrating over x and assuming $\lim_{x\to\pm\infty} f \to 0$ (for the sake of f being integrable), we obtain

$$-u(x)f(p,x) - D\frac{\partial f(x,p)}{\partial x} = \frac{u_1 - u_2}{3}\,\mathrm{div}_p(pf(0,p)) + C(p) \equiv Q(p). \tag{1.21}$$

In the last step, we denoted the RHS by $Q(p)$.

We now have a 1st order linear differential equation. The homogeneous solution should be found separately for:

- $x < 0$ (downstream): constant function $f = C(p)/u_2$ satisfies the above equation
- $x > 0$ (upstream): the solution reads

$$f(x,p) = \frac{Q(p)}{u_1} + K(p)\exp\left(-xu_1/D\right).$$

- from the continuity of $f(x,p)$ at the shock front we have $K(p) = C(p)/u_2$.

Bearing in mind the physical meaning of f as a number density of particles in a phase space it is clear that Q should be zero so that total number of particles is finite. This leads us to the condition

$$\frac{u_1 - u_2}{3}\frac{1}{p^2}\frac{\partial}{\partial p}\left(p^3 f(0,p)\right) + C(p) = 0, \tag{1.22}$$

where we wrote divergence in spherical coordinates in p-space. Substituting to the equation solution at the shock front $f(0,p) = C(p)/u_2$ we have an equation for $C(p)$

$$\frac{u_1 - u_2}{3} \frac{1}{p^2} \frac{\partial}{\partial p} \left(p^3 C(p)/u_2 \right) + C(p) = 0. \tag{1.23}$$

The possible solution is

$$C(p) = A p^{-\kappa}, \tag{1.24}$$

which we substitute to the eqn. 1.23, giving

$$\frac{u_1 - u_2}{3} \frac{A}{p^2} \left((3-\kappa) p^{2-\kappa} \right) + A p^{-\kappa} = 0.$$

Cancelling the momenta leads us to the solution for power-law exponent

$$\frac{u_1 - u_2}{3u_2}(3-\kappa) + 1 = 0$$
$$\kappa = \frac{3u_1}{u_1 - u_2} = \frac{3}{1 - 1/r},$$

For non-relativistic ideal plasma and the strong shock the value is $r = 4$, giving $\kappa = 4$. The result for the phase space distribution is

$$f(x,p) = A p^{-3r/(r-1)} \exp(-u_1 x / D). \tag{1.25}$$

The number of particles in the momentum interval $[p, p+dp]$ we obtain by the integration $f(x,p)$ over all possible velocity directions

$$N(x,p)dp = \int_0^{\pi} \int_0^{2\pi} p^2 \sin\theta f(x,p)\, d\theta\, d\phi\, dp = 4\pi p^2 f(x,p) dp \propto p^{-\kappa+2} dp. \tag{1.26}$$

Taking into account $E_{\mathrm{kin}} \propto p$

$$N(E,x) \propto E^{-s}. \tag{1.27}$$

The spectral index for the non-relativistic case then is

$$s = \kappa - 2 \doteq 2. \tag{1.28}$$

For the time evolution tracking, the above procedure should be performed, including the loss terms. For electrons, the relevant cooling processes are synchrotron cooling and relativistic bremsstrahlung, whereas, for protons, energy dissipation occurs, e.g., due to the proton-proton inelastic scattering.

Microscopic treatment

In section 1.3.2 we have derived the expression for the power-law exponent s. Afterward, we have evaluated its value from the transport equation. In this part, we will reconstruct the macroscopic number value result for s (eqn. 1.28) with a deeper insight to the microscopic processes. According to the eqn. 1.19, we see that

$$s = 1 - \frac{\ln P}{\ln A}. \tag{1.29}$$

Combining equations 1.17 and 1.13 we can find

$$\ln A = \ln\left(1 + \frac{4V}{3c}\right) \doteq \frac{4V}{3c} = \frac{U}{c}, \tag{1.30}$$

where U and V are defined in sec. 1.3.1. In the last step, we have used numerical values from the fig. 1.7, that are valid for the non-relativistic shock.

The parameter P is a return probability - the fraction of particles that crosses the shock back instead of being advected away in each step (see eqn. 1.15). In terms of the escape probability, we can write $P = 1 - P_{\mathrm{esc}}$. Firstly, we will calculate the number density of particles that enter the downstream region from the upstream per unit time $n_{\mathrm{enter}}/\Delta t$ and then we will compare this to the advection flux downstream $n_{\mathrm{esc}}/\Delta t$. The escape probability is then $P_{\mathrm{esc}} = n_{\mathrm{esc}}/n_{\mathrm{enter}}$.

For further derivation, we need to consider the following picture. We start in the upstream rest frame. There is some number of particles isotropically distributed with a given energy E_0.

We measure the angle at which particles cross the shock in terms of θ, which is measured from the shock normal pointing against the plasma flow (to the left on fig. 1.7 (c)). Consequently, as we are interested in the flux of the particles that will reach the downstream, we consider only those particles that have a positive projection on the θ-axis. The range of values is then $\theta \in [0, \pi/2]$. The angular dependence on ϕ will not have any physical consequences, so we consider only the projection of the velocity $v\cos\theta$. The set of all directions pointing from upstream to the downstream we denote in terms of the solid angle $\Omega_{1\to 2}$

$$\frac{n_{\mathrm{enter}}}{\Delta t} = \int_{\Omega_{1\to 2}} \frac{\rho_{\mathrm{CR}} c\cos\theta}{4\pi} d\Omega_{1\to 2} = \int_0^{2\pi}\int_0^{\pi/2} \frac{\rho_{\mathrm{CR}} c\cos\theta}{4\pi}\sin\theta d\theta d\phi \tag{1.31}$$

$$= \frac{\rho_{\mathrm{CR}} c}{2}\int_0^1 \cos\theta d\cos\theta = \frac{\rho_{\mathrm{CR}} c}{4}. \tag{1.32}$$

The rest of the calculations we perform in the shock rest frame. Both thermal and non-thermal particles are advected away with a velocity u_2. Then, using the solution of the eqn. 1.21 derived above, we know that the non-thermal density $\rho_{\mathrm{CR}} = \int f(x,p)dp$ is constant downstream, so we get $n_{\mathrm{esc}}/\Delta t = \rho_{\mathrm{CR}} u_2$. The probability of being advected away from the shock in the stationary non-relativistic case is

$$P_{\mathrm{esc}} = \frac{\rho_{\mathrm{CR}} u_2}{c\rho_{\mathrm{CR}}/4} = \frac{4u_2}{c}. \tag{1.33}$$

It gives us

$$\ln P = \ln\left(1 - \frac{4u_2}{c}\right) \doteq -\frac{4u_2}{c} = -\frac{U}{c}. \tag{1.34}$$

Combining equations 1.30, 1.34 and 1.29 we find

$$s \doteq 2, \tag{1.35}$$

which is consistent with the macroscopic results.

In case of the relativistic shock, the resulting spectrum appears to be steeper (e.g. Kirk et al. [2000]). Since the observed spectrum of CR is power-law with spectral index consistent with DSA prediction, we adopt DSA as a mechanism of particle acceleration in radiogalaxies.

Chapter 2

Synchrotron emission

2.1 Description of the sources

We perform our calculations on the four hotspots of the radiogalaxies 3C 105, 3C 227 and 3C 445. The high-resolution data unveiled a fine structure of the sources, from which we selected 8 subcomponents that we call knots hereafter. We use names of the sources assigned by the Third Cambridge Catalogue of Radio Sources (3CR). The radio measurements were performed by the Very Large Array (VLA), situated in the New Mexico.

We name the hotspots, and their components, according to the authors of the observational publications that we adapt figures from. For all sources we use measurements in radio regime.

Table 2.1: From left to right, we list the name of the source, the redshift (z), the scale (in kpc arcsec^{-1}), the distance (in Gpc), the radio spectral index α, the steepness of the relativistic electrons energy distribution $s = 2\alpha + 1$, and the proton to electron energy density ratio a.

Source	z	scale	d	α	s	a
3C 105	0.089	1.642	0.4017	0.8	2.6	4.51
3C 227	0.0861	1.62	0.3878	0.75	2.5	6.58
3C 445	0.0562	1.067	0.2479	0.75	2.5	6.58

3C 105

The radiogalaxy 3C 105 is hosted by the Narrow Line Radio Galaxy at redshift $z = 0.089$. The best available resolution at radio frequencies corresponds to the frequency 8.4 GHz. The observations were carried at the VLA. Three knots of the southern hotspot can be distinguished, that are denoted as S1, S2, and S3, respectively (see fig. 2.1), accompanied by a diffuse emission. The component S1 is interpreted as a jet emission [Leahy et al., 1997], whereas the components S2 and S3 are referred as a double hotspot, that could be formed by a disconnection event due to the deceleration caused by the ambient material [Cox et al., 1991].

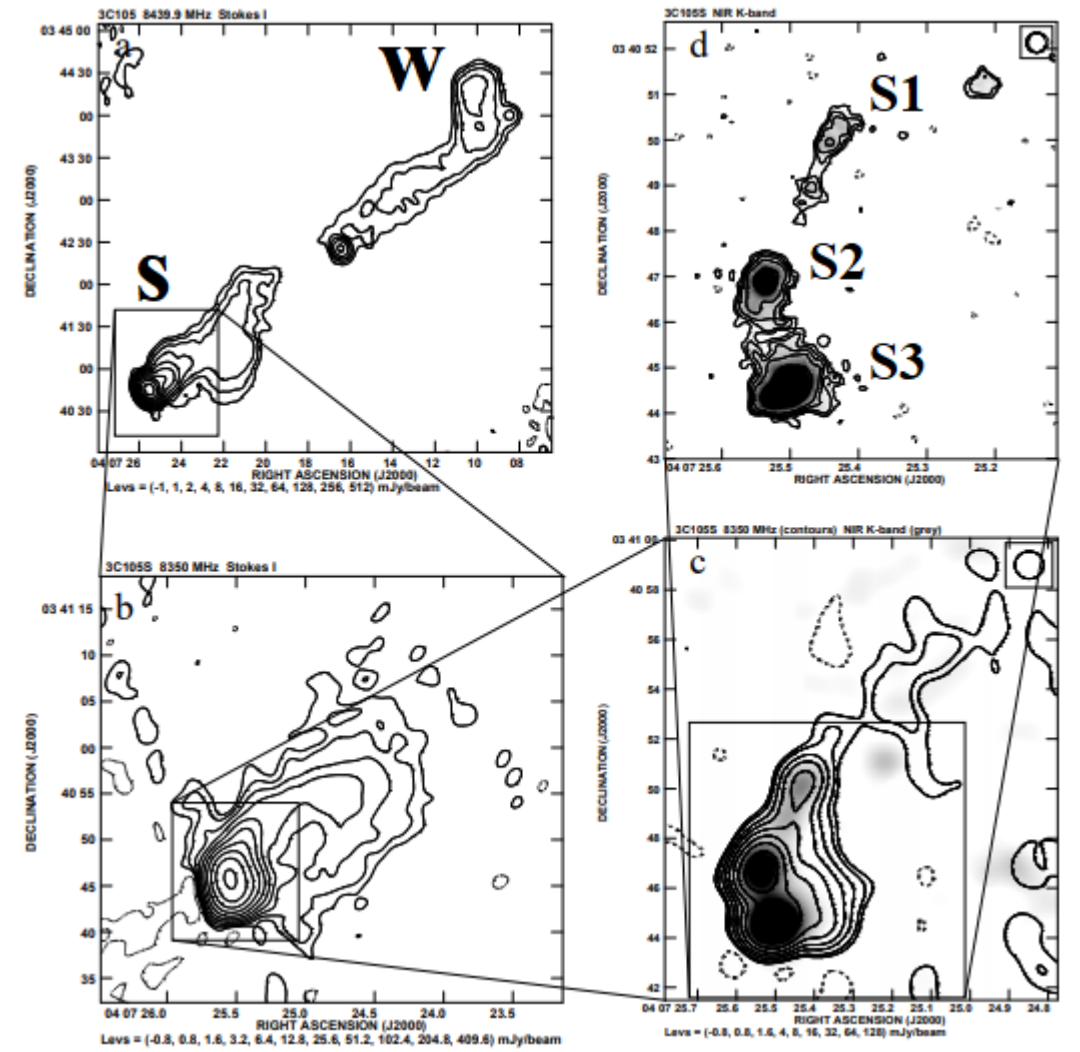

Figure 2.1: a) Jets of the radiogalaxy 3C 105 at $\nu = 8.3\,\mathrm{GHz}$ b) Its southern hotspot 3C 105 S at $\nu = 8.3\,\mathrm{GHz}$ c) VLA measurements combined with the ISAAC (VLT) measurements at K-band ($\lambda = 2.2\,\mu m$) d) Three resolved knots that are denoted as S1, S2 and S3 at $\lambda = 2.2\,\mu m$. Credit: [Mack et al., 2009].

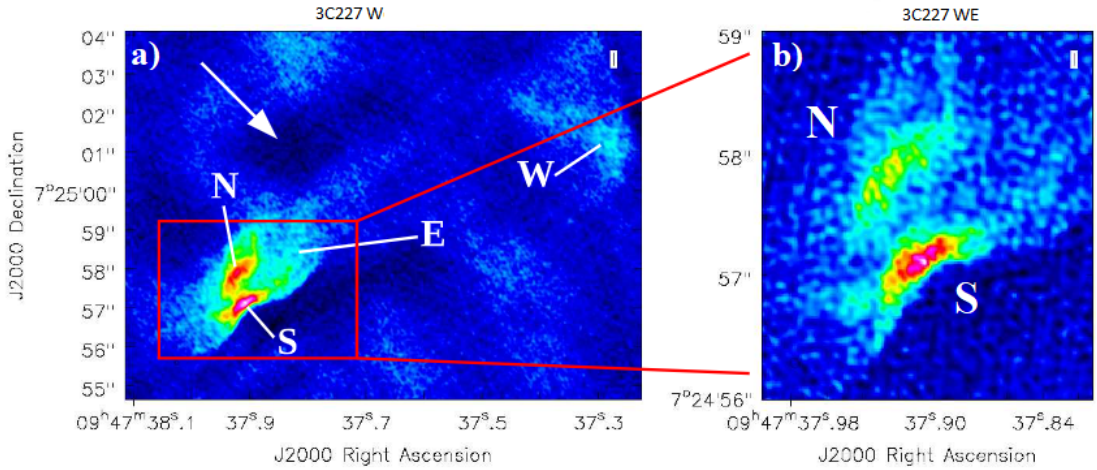

Figure 2.2: The western hotspot of the radiogalaxy 3C 227. Arrow points to the direction of the jet. a) Two knots - East (E) and West (W) are distinguished at frequency 22 GHz. b) The eastern knot of 3C 227 W consist of the northern and southern subcomponents. Credit: [Orienti et al., 2020].

3C 227

Another case of study is radiogalaxy 3C 227 located at $z = 0.0861$, which was observed by Jansky Very Large Array A-configuration at 22 GHz. For our calculations, we use data from both lobes, in particular the eastern hotspot 3C 227 E and the two knots of the western hotspot 3C 227 WN and 3C 227 WS that could have underwent the similar disconnection process as is supposed for 3C 105 S2 and S3 [Mack et al., 2009]. The western knots are elongated roughly transverse to the jet direction. The eastern knot consists of a single prominent hotspot (labled as HS in fig. 2.3) with a multiple fainter emission sources, that we exclude from the analysis.

3C 445

Radiogalaxy 3C 445 is located at redshift $z = 0.0562$. The data were collected at frequency 22 GHz by Jansky Very Large Array A-configuration (see fig. 2.4). For our research we selected the southern lobe. There are 2 resolved subcomponents, with eastern knot being responsible for about 50% brightness of the whole hotspot complex. The western knot is embedded in a widely spread diffuse emission, which we neglect in our calculations. Both of the knots are elongated roughly transverse to the jet direction.

Volume estimate

We estimate the volume of each knot using the high-resolution radio images of the hotspots (see fig. 2.5) that were taken from the literature. We have converted the numbers of pixels to areas of the knots, projected on the plane of the sky. To include the third dimension to the calculation, we assume this axis to be the same as the minor observed size of the knot. We calculate the volume of each knot $V = 2l_{\mathrm{min}}^2 l_{\mathrm{maj}}/3$ assuming the hotspot is an ellipsoid, with the two minor axes l_{min} and the major axis l_{maj}, calculated from the ellipsoid area.

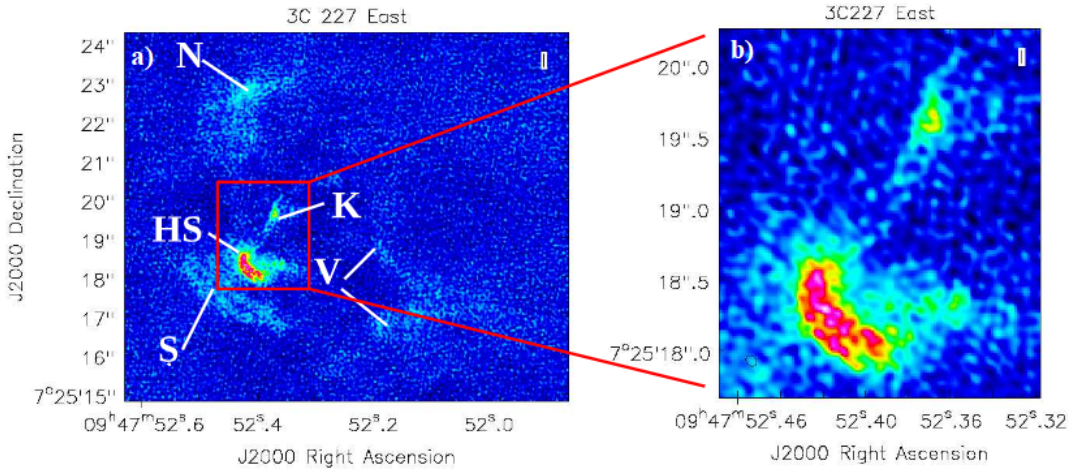

Figure 2.3: a) The eastern hotspot of the radiogalaxy 3C 227. b) The zoomed image of the selected knot that corresponds to the main hotspot emission. Credit: [Orienti et al., 2020].

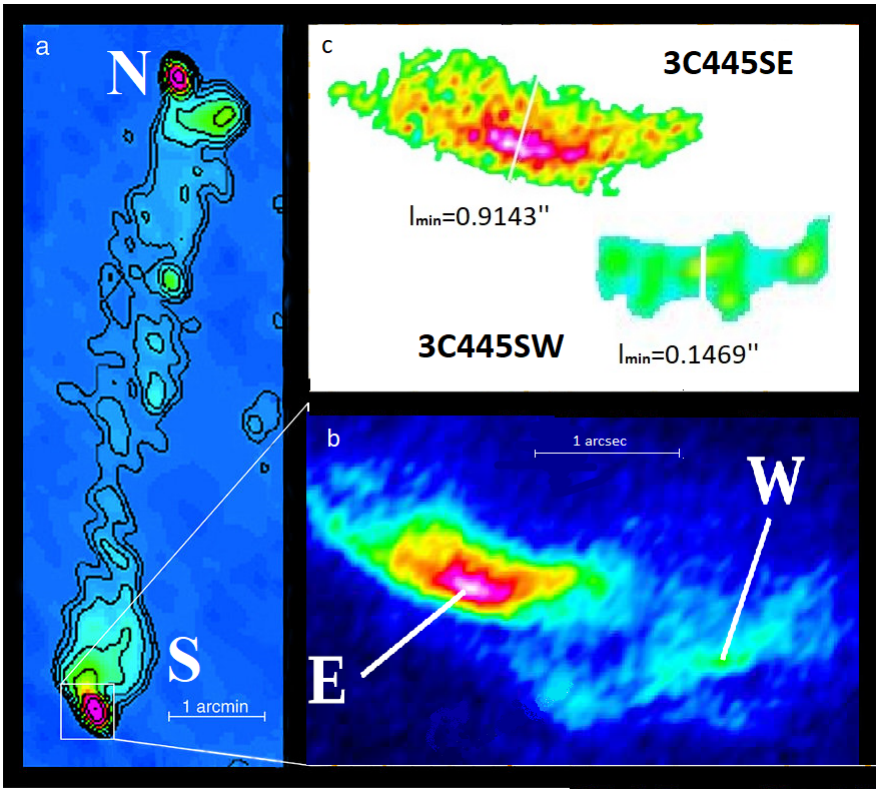

Figure 2.4: Radio galaxy 3C 455. (a) The snapshot observation of the whole galaxy and jets taken by Very Large Array (VLA) at 8.4 GHz. Credit: ESO. (b) Southern hotspot in radio 22 Hz. (c) The two separate emission regions (so-called knots) are resolved. Adapted from: [Orienti et al., 2020].

In case of radiogalaxy 3C 105, we use the fluxes at frequency $\nu = 8.4\,\mathrm{GHz}$ and the axes sizes from [Orienti et al., 2012].

Table 2.2: Observed and calculated parameters of hotspots. All quantities measured in pixels are obtained using fig 2.5. From left to right we list the name of the source and the non-thermal component in the jet, the area of the hotspot A and scale for the transition to the arcseconds, the minor axis l_{min} and the calculated volume filled in with non-thermal electrons V_e.

Source	Comp.	A [px^2]	scale [px/arcsec]	l_{min} [px]
3C 227	WS	19562	2/577	76
	WN	14064	2/577	67
	E	35914	1/310	110
3C 445	SE	28358	2/245	112
	SW	1767	2/245	18

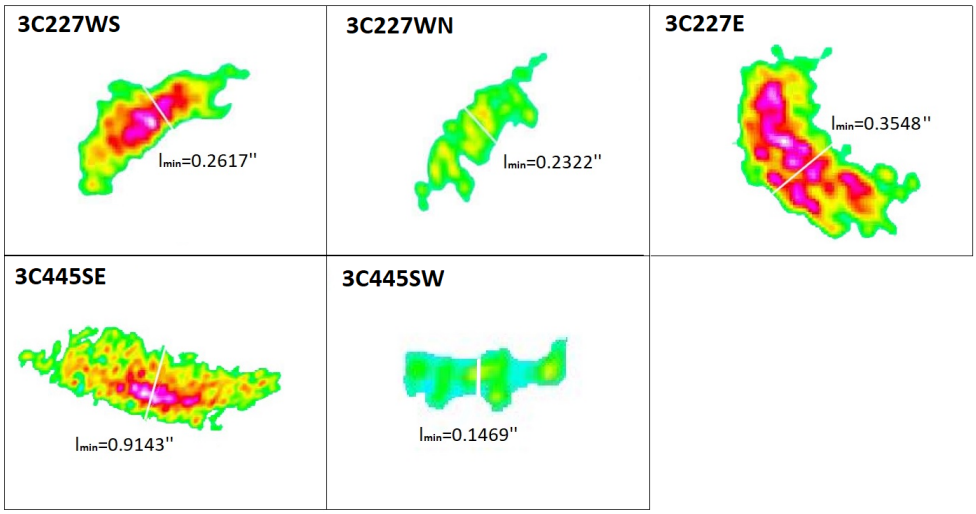

Figure 2.5: The hotspots of the selected AGNs at the best resolution. Adapted from: [Orienti et al., 2020].

2.2 Total energy density of non-thermal electrons

As was described in section 1.3.2, the DSA predicts the power-law spectrum for the cosmic rays as emitted by the source. A similar distribution is seemed to be applicable for both non-thermal electrons and protons [Longair, 2010, p. 30]. From the spectrum of the selected source, we can estimate the magnetic field that is a necessary ingredient for calculating the maximum energy of the non-thermal

Table 2.3: Observed and derived parameters of hotspots. From left to right we list the name of the source and the non-thermal component in the hotspot, the observed frequency ν and measured flux density S_ν, the angular sizes θ_{maj}, θ_{min} and minor axis l_{min}, the volume V and the cut-off frequency ν_{cut}.

Source	Comp.	ν [GHz]	S_ν [mJy]	$\theta_{\mathrm{maj}} \times \theta_{\mathrm{min}}$ [$''\times''$]	l_{min} [kpc]	V [kpc^3]	ν_{cut} [Hz]
3C 105	S1	8.4	18.4	1×0.8	1.31	1.484	$2 \cdot 10^{15}$
	S2	8.4	372	1.3×1	1.64	3.013	$3 \cdot 10^{14}$
	S3	8.4	260	1.5×0.8	1.31	2.225	$3 \cdot 10^{14}$
3C 227	WS	22	3.80	1.14×0.26	0.42	0.174	10^{15}
	WN	22	3.51	0.93×0.23	0.38	0.111	10^{15}
	E	22	8.15	1.34×0.35	0.57	0.375	$5 \cdot 10^{15}$
3C 445	SE	22	14.24	2.63×0.91	0.98	1.399	$2.6 \cdot 10^{15}$
	SW	22	2.92	1.02×0.15	0.16	0.014	$4.7 \cdot 10^{15}$

electrons. The non-thermal electron distribution for unit volume reads

$$N_e = K_e(s)E^{-s}. \tag{2.1}$$

Here $K_e(s)$ is the normalization function and E is the energy of the non-thermal electron in the jet plasma, and s is a power-law exponent.

Observing the hotspot, we detect a radiation flux S_ν in radio waveband that obeys a power-law in frequencies $S_\nu \propto \nu^{-\alpha}$. As can be seen from tab. 2.3, for our sources of interest, it holds $\alpha \geq 0.3$, which means that the emission has a non-thermal origin. The synchrotron emission appears when electrons gyrate along the magnetic field line at relativistic velocities. An ensemble of electrons with a power-law energy distribution 2.1 emits a power-law flux in frequencies $S_\nu \propto \nu^{-\alpha}$. We consider synchrotron emission to make the main contribution to the observed photon flux S_ν from the hotspot. For the synchrotron emission it holds [Lang, 2013]

$$s = 2\alpha + 1, \tag{2.2}$$

so from the radiation flux measurement we can get an estimate of the electrons spectral index s.

The normalization K_e we calculate from the synchrotron theory, described e.g. in [Beck and Krause, 2005], [Arbutina et al., 2012]. The synchrotron emissivity is defined as follows

$$\epsilon_\nu = 4\pi d^2 S_\nu V^{-1} := 4\pi\varepsilon_\nu, \tag{2.3}$$

where

$$\varepsilon_\nu = c_5 K_e (B\sin\theta)^{\frac{s+1}{2}} \left(\frac{\nu}{2c_1}\right)^{\frac{1-s}{2}}. \tag{2.4}$$

Here B is a magnetic field of the plasma in a hotspot, θ is an angle between the field lines and a particle velocity, ν is frequency. Below we list the constants used

in the last equation

$$c_1 = \frac{3e}{4\pi m_e^3 c^5} \doteq 6 \cdot 10^{18}\,\mathrm{erg}^{-2}\,\mathrm{s}^{-1}\,\mathrm{G}^{-1}$$
$$c_3 = \frac{\sqrt{3}e^3}{4\pi m_e c^2} \doteq 1.87 \cdot 10^{-23}\,\mathrm{erg}\,\mathrm{G}^{-1}\,\mathrm{sterad}^{-1}$$
$$c_5 = c_3 \Gamma\left(\frac{3s-1}{12}\right)\Gamma\left(\frac{3s+19}{12}\right)\frac{1}{s+1}.$$

As we are not interested in the angle distribution of the particles, we will average over the θ angle and replace

$$(\sin\theta)^{\frac{s+1}{2}} \to \left\langle (\sin\theta)^{\frac{s+1}{2}} \right\rangle_0^\pi.$$

Integration gives us[1]

$$\left\langle (\sin\theta)^{\frac{s+1}{2}} \right\rangle_0^\pi \equiv \frac{1}{\pi}\int_0^\pi \sin\theta^{\frac{s+1}{2}} d\theta = \frac{1}{\sqrt{\pi}}\frac{\Gamma\left(\frac{s+3}{4}\right)}{\Gamma\left(\frac{s+5}{4}\right)}. \tag{2.5}$$

Equating emissivities from the equations 2.3 and 2.4, we can determine the normalization K_e of the non-thermal energy distribution

$$K_e = \varepsilon_\nu B^{-\frac{s+1}{2}} \nu^{\frac{s-1}{2}} \frac{(2c_1)^{\frac{1-s}{2}}\sqrt{\pi}\Gamma\left(\frac{s+5}{4}\right)}{c_5\Gamma\left(\frac{s+3}{4}\right)}. \tag{2.6}$$

The numerical value of any present Γ-function is close to 1. Expressing emissivity in terms of the observed quantities, we find

$$K_e = \xi_K(s) d^2 S_\nu V^{-1} B^{-\frac{s+1}{2}} \nu^{\frac{s-1}{2}}, \tag{2.7}$$

where we have defined

$$\xi_K(s) = \frac{(2c_1)^{\frac{1-s}{2}}\Gamma\left(\frac{s+7}{4}\right)(s+1)}{4\sqrt{\pi}\Gamma\left(\frac{s+5}{4}\right)\Gamma\left(\frac{3s-1}{12}\right)\Gamma\left(\frac{3s+19}{12}\right)}. \tag{2.8}$$

Now we can proceed in determining values of the total[2] energy density of the non-thermal electrons $U_{\mathrm{e,tot}}$

$$U_{\mathrm{e,tot}} = \int N(E) E dE = \int K_e E^{-s+1} dE = K_e \frac{E_{\mathrm{e,max}}^{-s+2} - E_{\mathrm{e,min}}^{-s+2}}{-s+2}.$$

[1] In frequently cited book [Longair, 2010], the integration is performed using the formula

$$\frac{1}{2}\int_0^\pi (\sin x)^{\frac{p+3}{2}} dx = \frac{\sqrt{\pi}}{2}\frac{\Gamma\left(\frac{p+5}{4}\right)}{\Gamma\left(\frac{p+7}{4}\right)}.$$

We have noticed a typo, as the author used the above equation exactly as it is without a corresponding shift in the power $p+2 = s$. Numerical values of the resulting coefficient differ for 16%.

[2] Total here means that we integrate differential energy density over all energies.

For all the sources in our study, we have $s > 2$, and therefore we can neglect the term containing $E_{\mathrm{e,max}}$ since it is orders of magnitude greater than $E_{\mathrm{e,min}}$

$$U_{\mathrm{e,tot}} \approx K_e \frac{E_{\mathrm{e,min}}^{-s+2}}{s-2} := K_e f_e. \tag{2.9}$$

Hence, substituting this result from the eqn. 2.6 we have

$$U_{\mathrm{e,tot}} = \xi_K(s) \varepsilon_\nu B^{-\frac{s+1}{2}} \nu^{\frac{s-1}{2}} \frac{E_{\mathrm{e,min}}^{-s+2}}{s-2}. \tag{2.10}$$

We assume $E_{\mathrm{e,min}} = 50\, m_e c^2$ for electrons and $E_{\mathrm{p,min}} = 50\, m_p c^2$ for protons, where m_e and m_p are masses of electron and proton, respectively. These quantities correspond to the energy where the thermal (Maxwell-Boltzmann) distribution breaks into the power-law distribution. Since our analysis concerns only non-thermal particles, the transition point corresponds to the minimum energy distributed according to the power-law.

The final unknown ingredient that separates us from estimating the maximum energy of the non-thermal electrons is the magnetic field of the hotspot, which is the subject of study of the next section.

2.3 Magnetic field determination

2.3.1 Minimum magnetic field estimation

The kinetic energy density of the jet plasma $U_{\mathrm{kin}} = \rho c^2(\Gamma - 1) \approx 9 \cdot 10^{-9}\,\mathrm{erg\,cm^{-3}}$ plays a role of an energy budget for the hotspot because there is no other source of energy except for the incoming plasma flow. This energy is distributed between the thermal and non-thermal particles (U_{T} and U_{NT} energy density, respectively) as well as the magnetic field (U_{mag}). This can be written as

$$U_{\mathrm{kin}} \geq U_{\mathrm{T}} + U_{\mathrm{NT}} + U_{\mathrm{mag}}. \tag{2.11}$$

In the following calculation we neglect the energy density of thermal particles, as $U_{\mathrm{T}} \ll U_{\mathrm{NT}}$. The equation 2.11 then reads

$$\rho c^2(\Gamma - 1) \geq (1 + a)\tilde{K}_e f_e B^{-\frac{s+1}{2}} + \frac{B^2}{8\pi}. \tag{2.12}$$

Assuming the equality in the eqn. 2.12, the numerical solution gives us the minimum possible magnetic field ($min\, B$) for a hotspot. Graphically the qualitative solution is depicted in fig. 2.6. These calculated values are listed in tab. 2.4 and are used as the lower boundaries for the magnetic field in plot 2.7. For our calculations we consider $n_i = \rho/m_p = 10^{-4}\,\mathrm{cm^{-3}}$.

2.3.2 Equipartition magnetic field

There are three main methods of magnetic field determination. These are based on Zeeman effect, Faraday rotation, and the equipartition [Arbutina et al., 2012]. Here we will focus on the latter one.

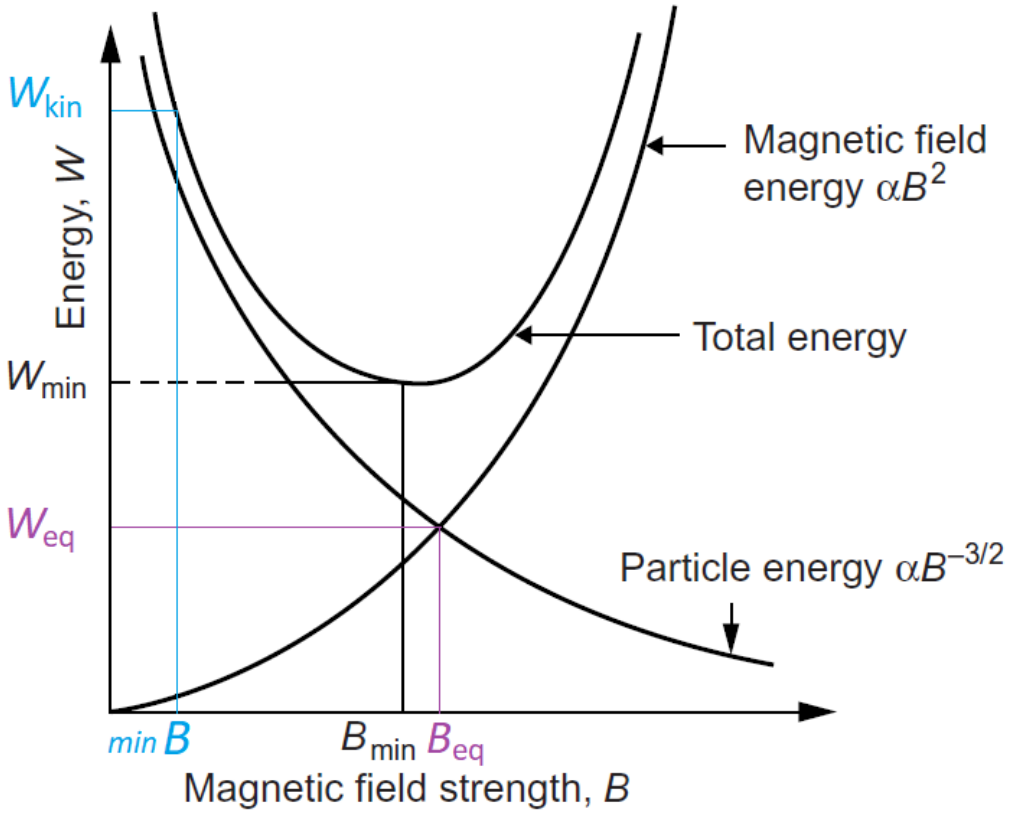

Figure 2.6: The equipartition magnetic field B_{eq} is a value that corresponds to the equal portion of energy W_{eq} distributed to the magnetic field and the particles. It appears to be the maximum reachable value of the magnetic field in a hotspot. As can be seen, this value is very close to the so-called 'minimum magnetic field' B_{min}, that *minimise the total energy* W_{min}. The minimum possible value of B in a hotspot is restricted by the jet kinetic energy W_{kin}. The corresponding field is denoted by $min\,B$. Adapted from: [Longair, 2010].

The equipartition assumption is that the energy in the magnetic field has the same value as the energy in the non-thermal particles (the thermal energy density is negligible). It worth mentioning that the equipartition magnetic field B_{eq} is frequently called 'minimum magnetic field' B_{min}, which could be rather misleading. By minimum magnetic field is meant the magnetic field that minimizes the total energy of particles and magnetic field. From fig. 2.6 it is clear, that B_{eq} and B_{min} indeed have similar values. Ironically, the equipartition magnetic field is the upper limit for the hotspot's magnetic intensity values.

As is shown above, an energy density of the non-thermal electrons is the power-law in magnetic field

$$U_{e,tot}(B) \propto B^{-\frac{s+1}{2}}.$$

For protons it holds

$$U_{p,tot} = aU_{e,tot}, \tag{2.13}$$

where $a = (m_p/m_e)^{(3-s)/2}$ (see tab. 2.3). Thus, the energy density of non-thermal particles is

$$U_{NT} = U_{p,tot} + U_{e,tot} = (1+a)U_{e,tot}. \tag{2.14}$$

We first write the equation for the $B_{\mathrm{eq,e}}$ under assumption that the magnetic field is in equipartition with a non-thermal electrons only

$$\frac{B_{\mathrm{eq,e}}^2}{8\pi} = U_{\mathrm{e,tot}} = \xi_K(s)\varepsilon_\nu B_{\mathrm{eq,e}}^{-\frac{s+1}{2}} \nu^{\frac{s-1}{2}} \frac{E_{\mathrm{e,min}}^{-s+2}}{s-2}. \tag{2.15}$$

The magnetic field with equipartition only with non-thermal electrons reads

$$B_{\mathrm{eq,e}} = \xi_{\mathrm{eq}}(s)\varepsilon_\nu^{\frac{2}{s+5}} \nu^{\frac{s-1}{s+5}}, \tag{2.16}$$

where we have denoted

$$\xi_{\mathrm{eq}}(s) = (8\pi f_e \xi_K(s)^{\frac{2}{s+5}}. \tag{2.17}$$

The magnetic field in equipartition with both protons and electrons can be expressed as follows

$$B_{\mathrm{eq}}^2 = 8\pi U_{\mathrm{NT}} = 8\pi(U_{\mathrm{p,tot}} + U_{\mathrm{e,tot}}) = 8\pi(1+a)U_{\mathrm{e,tot}} = (1+a)B_{\mathrm{eq,e}}^2. \tag{2.18}$$

Solving the eqn. 2.15 and combining the result with eqn. 2.18 we calculate the equipartition magnetic field in our cases of study. The resulting values are listed in the tab. 2.4 and are also used as upper values in fig. 2.7. The magnetic field is crucial for the determination of the maximum energy of electrons. We plot the electron energy density $U_{\mathrm{e,tot}}$ as a function of a hotspot's magnetic field for all sources of interest in fig. 2.7.

Even though B_{eq} is the maximum possible energy of the particles in hotspots, the conditions for its occurrence are not extreme. As can be seen from fig. 2.6, it minimizes the total energy of the system, making this state preferable. Although we can not be sure if a given system reached equipartition, it seems to be a plausible assumption that we adopt hereafter.

Comparing these values to the predicted in numerical simulations [Casse and Marcowith, 2005], we see that to have a comprehensive model of the CR acceleration in hotspots we have to provide a mechanism of the sufficient magnetic field amplification. We dedicate a chapter 3 to this.

2.4 Maximum energy of the non-thermal electrons

Cutoff frequency

The maximum energy of the non-thermal electrons can be extracted from observations by means of a so-called cutoff frequency. The emission spectrum of the hotspots is considered to be most of the synchrotron origin of electrons. The observed spectra gradually decrease up to the so-called cutoff frequency ν_c, where the emission vanishes. We study it in more details in sec. 2.5. To determine the cutoff, we use fig. 2.8. For every single knot of the hotspot, the flux at different frequencies should be measured. The maximum frequency is the estimated value of the ν_c.

We have used such images for the knots of the hotspot 3C 227. For other sources, the cutoff frequencies were taken from literature [Orienti et al., 2012]. The list of the used values can be found in tab. 2.3.

Table 2.4: From left to right, we list the name of the source and the non-thermal component in the hotspot, the integral number density of the non-thermal electrons, the normalization function of the non-thermal electron energy distribution, the minimum magnetic field *min B*, the equipartition magnetic field $B_{\rm eq}$, and the maximum energy of the non-thermal electrons $E_{e,\rm max}$.

Source	Comp.	$U_{e,\rm tot}$ $[\rm erg\,cm^{-3}]\cdot 10^{-9}$	K_e $[\rm erg^{s-1}\,cm^{-3}]\cdot 10^{-12}$	*min B* $[\mu\rm G]$	$B_{\rm eq}$ $[\mu\rm G]$	$E_{e,\rm max}$ [TeV]
3C 105	S1	0.76	1.06	92	324	0.62
	S2	1.77	2.48	278	496	0.19
	S3	1.72	2.40	260	488	0.20
3C 227	WS	0.77	2.48	113	384	0.40
	WN	0.94	3.02	142	423	0.38
	E	0.77	2.47	112	383	0.90
3C 445	SE	0.32	1.02	44	247	0.81
	SW	1.6	5.12	332	552	0.73

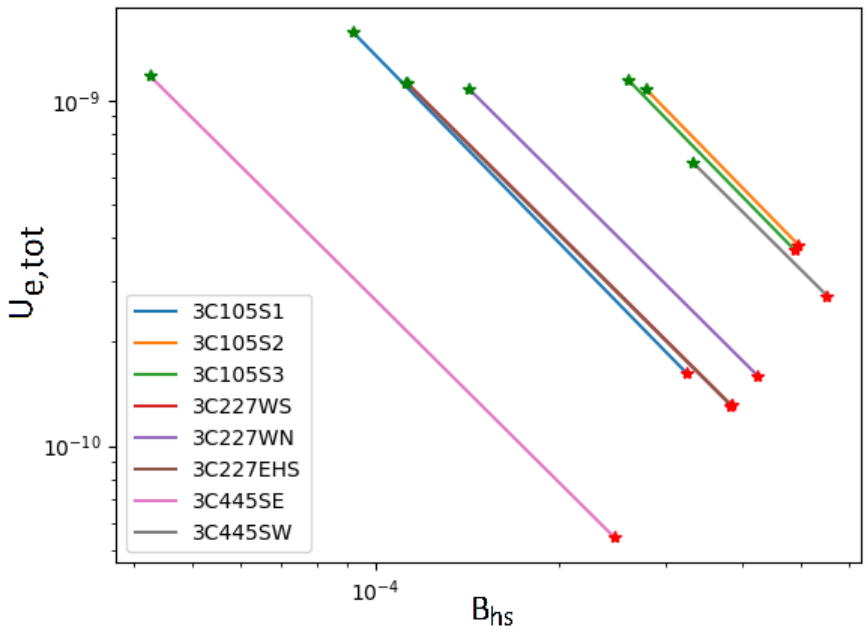

Figure 2.7: The log-log plot of a total energy density in non-thermal electrons in range from *min B* (green stars) to $B_{\rm eq}$ (red stars). Curves from sources 3C 227 WS and 3C 227 E HS are overlapping.

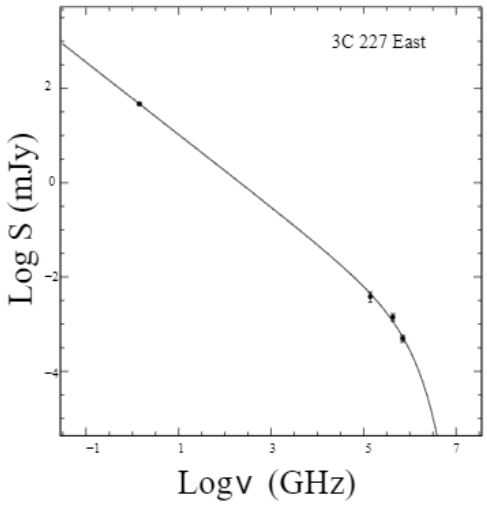

Figure 2.8: Emission of the eastern hotspot of the radiogalaxy 3C 227. Dots correspond to the measured photon flux at a given frequency. Curve corresponds to the model of the synchrotron emission. The maximum frequency correspond to the cutoff ν_c. Credit: [Mack et al., 2009].

Maximum energy

The synchrotron radiation (also called magnetobremsstrahlung radiation) of a single electron is primarily beamed in the transverse direction to the external magnetic field B. The emitted spectrum is continuous with a flux peak that occurs at $\nu = 0.3\,\nu_{\rm crit}$ of the so-called critical frequency (see. [Lang, 2013, p. 29]), given by

$$\nu_{\rm crit} = \frac{3qB}{4\pi m_e c}\Gamma^2 \sin\theta, \tag{2.19}$$

where Γ is a Lorentz factor of electron, q is an electron charge, and θ is a pitch angle. The emission of the electron ensemble will eliminate the dependence on θ. We can introduce the dependence on energy by is $\Gamma = E/(m_e c^2)$. Now, using the cutoff frequency from the previous section we can calculate the maximum energy of the non-thermal electrons in a given source, assuming the magnetic field is known

$$E_{\rm e,max} = \sqrt{\frac{4\pi m_e c}{3q}} m_e c^2 \sqrt{\frac{\nu_c}{B}} \equiv C_e \sqrt{\frac{\nu_c}{B}}. \tag{2.20}$$

We assume all non-thermal protons and electrons to be in equipartition with both initial and perturbed magnetic fields for our calculations, namely $B = B_{\rm eq}$. The results are listed in tab. 3.1.

In the next section we give a closer look to the synchrotron spectrum has a cutoff.

2.5 Maximum energy of the non-thermal electrons is not determined by synchrotron cooling

2.5.1 Diffusion coefficient assuming the cutoff occurs due to synchrotron cooling

Observational evidence clearly shows that the synchrotron spectrum is limited from above. One of the standard approaches in an effort to reveal the physics behind the existence of such cutoff is to assign a key role to synchrotron cooling. If the cooling is more effective than the acceleration, the energy of a particle will decrease. The maximum energy is then given by a condition of equality of the acceleration and cooling rates

$$\dot{E}_{\rm synch}(E_{\rm e,max}) = -\dot{E}_{\rm acc}(E_{\rm e,max}). \tag{2.21}$$

Here we denote a time derivative by a dot. Taking into account that both acceleration and cooling time can be expressed as $t = -E/\dot{E}$, for electrons, it is equivalent to the condition

$$t_{\rm acc}(E_{\rm e,max}) = t_{\rm synch}(E_{\rm e,max}), \tag{2.22}$$

which represents the assumption of synchrotron cooling to be the reason of an electron maximum energy cutoff. Following the procedure presented in [Araudo et al., 2016], we firstly use the above equation to express the diffusion coefficient for the scenario when synchrotron cooling determines the maximum energy of electrons in the hotspots.

According to the standard result for the synchrotron cooling of an electron (e.g., see [Longair, 2010])

$$t_{\rm synch} = -\frac{E}{\dot{E}} = \frac{3E}{4\sigma_T c U_B \beta^2 \gamma^2} = \frac{3\gamma m_e c^2}{4\sigma_T c U_B \beta^2 \gamma^2} = \frac{6\pi m_e c^2}{\sigma_T c B^2 \beta^2 \gamma}, \tag{2.23}$$

where $\beta = v/c$, v is the velocity of the particle, U_B is a magnetic energy density, γ is a Lorentz factor and the Thompson cross-section is

$$\sigma_T = \frac{8\pi}{3}\left(\frac{e^2}{m_e c^2}\right)^2. \tag{2.24}$$

Here we have assumed the relativistic particles, so that $\beta = 1$. Substituting there the maximum energy we get

$$t_{\rm synch} = \frac{7.8 \cdot 10^8}{\gamma_c B^2}, \tag{2.25}$$

where we denote the Lorentz factor for the cutoff energy as

$$\gamma_c \equiv \frac{E_{\rm e,max}}{m_e c^2}. \tag{2.26}$$

Another important ingredient is the acceleration time $t_{\rm acc}$. In case of perpendicular shock, the plasma density is compressed by a factor r downstream comparing

to the upstream. As we show in sec. 1.2.1, perpendicular configuration assumption is valid for our case of the hotspot RS. Due to the compression downstream, the diffusion coefficient also changes at the shock so that $D_1 = rD_2$. A time that would take for the particle to make a round trip, crossing the shock and back, is given by

$$t_{\rm cycle} = \frac{4}{c}\left[\frac{D_1}{u_1} + \frac{D_2}{u_2}\right] = \frac{4}{c}\left[\frac{D_1}{U} + \frac{D_1/4}{U/4}\right] = \frac{8}{c}\frac{D_1}{U}. \tag{2.27}$$

We have used $u_1 = U$, $u_2 = U/4$ as follows from fig. 1.7. We kept the notation regarding subindices, namely '1' corresponds to the upstream and '2' to the downstream values. Taking eqn 1.13 and considering $\Delta t \equiv t_{\rm cycle}$

$$t_{\rm acc} = \frac{E}{\dot{E}} \doteq E\frac{\Delta t}{\Delta E} = \frac{E}{\Delta E}t_{\rm cycle} = \frac{c}{U}t_{\rm cycle} = \frac{8D_1}{U^2}. \tag{2.28}$$

Substituting equations 2.25, 2.28 to 2.22 we have the expression for the diffusion coefficient provided that the synchrotron cooling rate is as high as the acceleration rate

$$D_{\rm synch} = \frac{U^2}{8}t_{\rm synch}. \tag{2.29}$$

Using eqn. 2.25 we find

$$D_{\rm synch} = \frac{U^2}{8}\frac{7.8\cdot 10^8}{\gamma_c B^2} = \frac{7.8\cdot 10^8}{8}\frac{U^2 m_e c^2}{E_{\rm e,max}B^2} = 80\frac{U^2}{E_{\rm e,max}B^2} = 2\cdot 10^{11}U^2\nu_c^{-\frac{1}{2}}B^{-\frac{3}{2}}. \tag{2.30}$$

Now, we will implement the additional requirements for the diffusion coefficient.

2.5.2 Upper limit for the diffusion coefficient

General formulas for determining the diffusion coefficient are

$$D = \lambda\frac{c}{3}, \qquad\qquad \lambda = \frac{r_g^2}{S}, \tag{2.31}$$

where λ is mean free path and S is the characteristic size of the magnetic field turbulence.

We have discussed in the preceding chapter that for effective acceleration, we need particles to cross the shock multiple times. Due to the diffusion of the particles away from the shock, a particle can leave the shock vicinity and will not undergo further acceleration. We can explore the range of possible diffusion coefficients by introducing physical limits on the characteristic turbulence scale in the plasma

$$c/\omega_{pi} \le S \le r_g. \tag{2.32}$$

The term c/ω_{pi} is ion skin depth, and ω_{pi} is proton plasma frequency. The lower bound represents that the plasma turbulence cell can not be smaller than the ion skin depth. This condition follows from the ion plasma frequency being the highest possible wave frequency capable of propagating in the plasma. The wavelength of the wave in plasma then determines the characteristic turbulence cell size. We will adapt the lower bound and examine the implications of such a choice. The plasma frequency is given by

$$\omega_{pi}^2 = \frac{4\pi q^2 n}{m_p\gamma_p} \Rightarrow S_{\rm min} \equiv \frac{c}{\omega_{pi}} = c\sqrt{\frac{m_p\gamma_p}{4\pi q^2 n}}.$$

We denoted the ion number density in the jet as n. Hereafter, we assume a Lorentz factor of jet plasma $\gamma_p = 1$. The Larmor radius corresponding to the synchrotron cutoff energy $r_g = r_g(\gamma_c)$ reads

$$r_g(\gamma_c) = \frac{E_{\rm e,max}}{qB_{\rm eq}} = \sqrt{\frac{2\pi m_e}{q}} m_e c^2 \sqrt{\frac{\nu_c}{B_{\rm eq}}} \frac{1}{qB_{\rm eq}} = m_e c^2 \sqrt{\frac{2\pi m_e}{q^3 B_{\rm eq}^3}} \sqrt{\nu_c}. \tag{2.33}$$

Using equations 2.31, 2.33 we find the expression for the diffusion coefficient at the cutoff energy

$$D_{\rm max}\left(E_{\rm e,max}\right) = \lambda_{\rm max}\frac{c}{3} = \frac{r_g^2(\gamma_c)}{S_{\rm min}}\frac{c}{3} = \frac{r_g^2(\gamma_c)}{c/\omega_{pi}}\frac{c}{3} = \frac{r_g^2(\gamma_c)}{3}\omega_{pi} = \frac{E_{\rm e,max}^2}{3q^2B^2}\omega_{pi}. \tag{2.34}$$

We are now ready to derive the restriction for the ion number density in the jet.

2.5.3 Ion number density in the jet

Since eqn. 2.34 represents the upper limit for a diffusion coefficient that contains no assumptions but only the fundamental constraint from a plasma physics, any valid diffusion coefficient will not exceed $D_{\rm max}$

$$D_{\rm max}^2(E_{\rm e,max}) \geq D_{\rm synch}^2 \Rightarrow \frac{E_{\rm e,max}^4}{9q^4B^4}\omega_{pi}^2 \geq \left(\frac{7.8\cdot 10^8}{8}\frac{U^2 m_e c^2}{B^2 E_{\rm e,max}}\right)^2.$$

Denoting $A = 7.8/8 \cdot 10^8$, we find

$$\frac{E_{\rm e,max}^6}{9q^4}\omega_{pi}^2 \geq A^2U^4m_e^2c^4$$
$$\frac{4\pi q^2 n}{m_p} \geq \frac{9A^2U^4m_e^2c^4q^4}{E_{\rm e,max}^6}.$$

The allowed range for the ion number density in the jet is

$$n \geq \frac{9A^2U^4m_pq^5}{4(4/3)^3m_e^7c^{11}\pi^4}B^3\nu_c^{-3} = 4\cdot 10^{17}U^4B^3\nu_c^{-3} \equiv n_{\rm min}. \tag{2.35}$$

Assumption of the equality between $D_{\rm synch}$ and $D_{\rm max}(E_{\rm e,max})$ leads us to the minimum number density of the plasma $n_{\rm min}$. As an example of the typical values of the number density in similar system we can take $2\cdot 10^{-4}\,{\rm cm}^{-3}$ [Dreher et al., 1987] as an upper limit for in the western hotspot of Cygnus A, and $6\cdot 10^{-5}\,{\rm cm}^{-3}$ as an upper limit for the 3C 273 [Meisenheimer and Heavens, 1986]. We see from the fig. 2.9 that the values we obtain are unreasonably large for the radiogalaxies. This gives us a solid argument to doubt that the distribution of non-thermal electrons has a maximum energy cutoff due to the synchrotron cooling. For stating that the DSA is responsible for the CR acceleration in AGNs, we should find another mechanism that would predict the synchrotron spectrum cutoff. Araudo et al. [2016] and Araudo et al. [2018] proposed an alternative explanation, suggesting that the reason for the electron maximum energy cutoff in the hotspots of radiogalaxies the escape of electrons downstream of a quasi-perpendicular shock. This assumption has a noteworthy consequences for the CR maximum energy, that we will discuss in the following section.

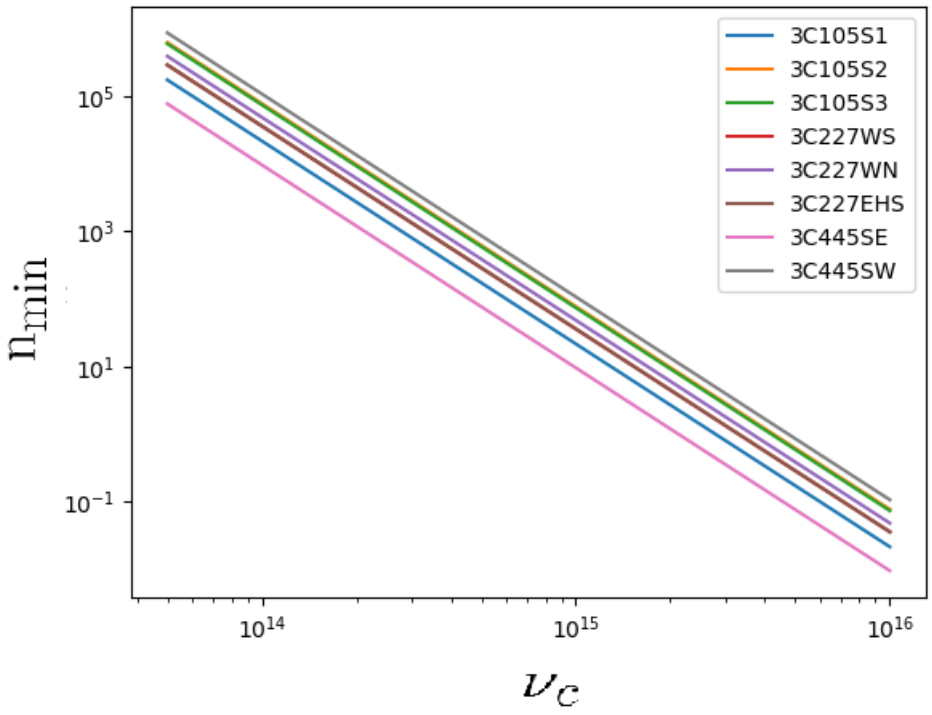

Figure 2.9: The log-log plot of a lower limit of the ion number density n_{min} of the jet for the cutoff frequencies ν_c in the vicinity of typical values $\nu_c \in [10^{14} - 10^{15}$ Hz], taken from [Orienti et al., 2012]. We use $B = B_{\mathrm{eq}}$. Curves are overlapping in pairs (3C 105 S2 with 3C 105 S3) and (3C 227 E HS with 3C 227 WS). We assume the shock velocity $U = c/3$.

2.6 Maximum energy of the non-thermal protons

In the previous sections, we have found the values of the maximum energy of the non-thermal electrons $E_{\mathrm{e,max}}$ for our set of radiogalaxies. We have also discovered that there should be another mechanism besides the synchrotron cooling that has to prevent particles from the higher energies. We assume that the reason for it is an early escape of the particles. We shall introduce relevant terminology and the derivation of the consequences of such assumptions for the maximum energy of CR.

2.6.1 Escape time

The particle can escape the DSA region either upstream or downstream. In the perpendicular magnetic field configuration, a particle is more likely to escape downstream than upstream. If the particle becomes magnetized at a distance of at least one Larmor radius away from the shock, it will follow the magnetic field line parallel to the shock front and will have no chance of crossing the shock again. This time is given by the advection time

$$t_{\mathrm{esc}\perp} = \frac{r_{g0}}{v_a}, \tag{2.36}$$

where $r_{g0} = E/(qB_0)$ is Larmor radius in unperturbed magnetic field B_0. The advection velocity $v_a = c$ in our calculations, since the RS is relativistic. We assume that the magnetization downstream of the shock determines the end of the acceleration process.

2.6.2 Maximum energy

Since we have chosen an escape of non-thermal electrons due to the magnetization downstream of the RS to be the limiting factor for the maximum energy of electrons in a perpendicular configuration, we should discuss how magnetization affects non-thermal protons. The escape condition for them (see eqn. 2.36) is exactly the same as for the electrons, as their Larmor radii are equal. Hence, particles would escape after the same time $t_{\mathrm{esc}\perp}$ at the same maximum Larmor radius r_g and, consequently, at the same maximum energy

$$E_{\mathrm{p,max}\perp} = E_{\mathrm{e,max}}. \tag{2.37}$$

As can be seen from the tab. 3.1, the resulting maximum energy is of the order of TeV that is far below the UHECR energies. We conclude that the hotspots of radiogalaxies most likely can not be sources of UHECR.

Chapter 3

Magnetic field amplification

In the previous chapter, we have estimated the magnetic field $B_{\rm eq}$ values in the hotspots, that occur to be orders of magnitude higher than those simulated in [Casse and Marcowith, 2005]. Hence, we need the magnetic field amplification on the RS that to be included in the comprehensive model of particle acceleration in the hotspot. In this chapter, we focus on the way how the acceleration can support the amplification of the magnetic field downstream up to the estimated values.

3.1 Instability growth

As we have argued in the sec. 1.3, scattering centers are needed in both upstream and downstream to ensure the repeated crossing of the shock front by the cosmic rays, as required for the DSA. The role of such scattering centers can play waves that occur in plasma naturally due to the propagation of the CR. When highly energetic particles (we consider protons) transit from downstream to upstream, they excite waves of different wavelengths. Moreover, the streaming of plasma particles supports a transfer of their energy to the turbulence inducing the amplitude growth of the waves. The propagation of the shock makes the upstream instabilities spread downstream ensuring presence of the scattering centers on both sides of the shock. The most effective scattering of the particles occurs due to the Alfvén waves, whose wavelength is similar to the CR Larmor radius [Bell, 1978]. We call these modes resonant.

The observations of the synchrotron emission indicate that the cooling process is very effective, and to achieve this, a strong magnetic field is needed (see sec. 2.3.2). The expected magnitude of the magnetic field is of the order of 100s μG downstream of the shock, whereas the average intensity in the jet is only around 1 μG [Casse and Marcowith, 2005]. The Alfvén waves can amplify magnetic field instabilities δB up to the values of the unperturbed field $\delta B \sim B_0$, which is insufficient to explain the observed synchrotron emission.

Bell [2004] argues that the magnetic field amplification happens due to the growth of the turbulence in plasma. Author introduced a new term $-\mathbf{j_{CR}} \times \mathbf{B}/c$ to the MHD equations. The perturbative solution appeared to be a set of waves of a different wavelengths. The dispersion relation for these CR-excited waves was derived (see fig. 3.1). It was shown that the dominant waves are not Alfvén, as can be seen from the maximum of the imaginary part of the dispersion relation. This

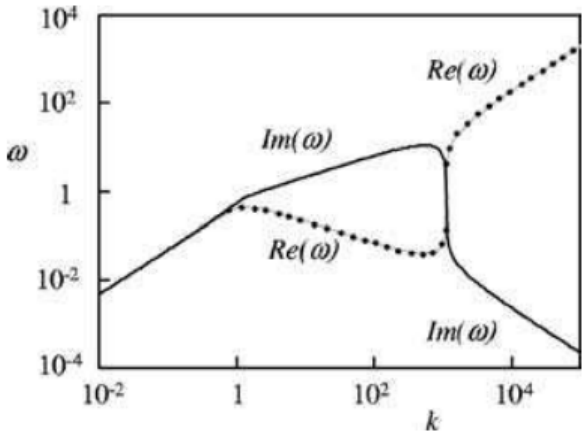

Figure 3.1: The dispersion relation for the maximum growth rate (k is in units of r_{g1}^{-1} and ω is in units of $v_{\rm sh}^2/cr_{g1}$, where r_{g1} is a Larmor radius of CR that underwent acceleration process). The $k = 1$ corresponds to the resonant Alfvén waves. The peak is the maximum growth rate of the NRH instabilities. Credit: [Bell, 2004].

new kind of instabilities is called Non-Resonant Hybrid instabilities (NRH) or, alternatively, Bell instabilities. The term 'non-resonant' corresponds to the fact that the characteristic wavelength of this kind of instability is not the Larmor radius of the accelerating particles. The amplification of the magnetic field is thus less likely to saturate at $\delta B \sim B_0$. 'Hybrid' refers to the fact that both particle-in-cell and MHD methods are coupled together.

This kind of instabilities appears in perpendicular configuration owing to the CR current density $j_{\rm CR}$ that occurs due to the pressure gradient on the shock (so-called diamagnetic drift). The current is orthogonal to both unperturbed magnetic field $\mathbf{B}_0$ and the shock normal $\mathbf{n}$. A maximum growth rate for the NRH instabilities is given by

$$\Gamma_{\rm NRH} = \max \mathrm{Im}(\omega) = 0.5\, j_{\rm CR} \sqrt{\pi/\rho_j}. \tag{3.1}$$

Here $\mathrm{j_{CR}}$ is the cosmic rays current and ρ_j is the density of the plasma in the jet. For the maximum magnetic field amplification, we will choose the instabilities with the highest growth rate 3.1.

3.2 Unperturbed magnetic field from the relevant timescales

With this growth rate, it is possible to explore the evolution of amplification. In [Bell et al., 2013] authors introduced a simulation, where they discovered that the magnetic field growth saturates after 5-10 e-foldings:

$$\Gamma_{\rm NRH} t \geq 5 - 10, \tag{3.2}$$

where $\Gamma_{\rm NRH}$ is maximum growth rate of NRH instabilities (see eqn. 3.1). The simulation started with randomly distributed seed NRH instabilities, growing

due to the CR of fixed energy propagating in the plasma. Physically, saturation starts when the characteristic size of the turbulence S grows up to the size of the Larmor radius r_g of a CR. After this moment, the individual instabilities that used to grow freely start mixing with the neighboring turbulence, which dramatically limits the further growth. This moment is called saturation of the linear regime. After this point, the magnetic field grows slower until it reaches its non-linear saturation.

Interestingly, the condition

$$S = r_g \tag{3.3}$$

corresponds to the so-called Bohm diffusion. It is the slowest possible diffusion of the charged particles in the plasma with an external magnetic field. The slower is diffusion, the more particles stay in the shock vicinity and thus are available for the DSA. Hence, the Bohm diffusion set the optimal acceleration regime. It is given by the condition, that the mean free path λ equals to the Larmor radius of the particle

$$\lambda_B = r_g. \tag{3.4}$$

Given that the mean free path is defined as

$$\lambda = \frac{r_g^2}{S}, \tag{3.5}$$

we obtain the linear saturation condition (eqn. 3.3).

Our case slightly differs from simulations discussed above, since we have CR of different energies simultaneously. Nevertheless, the eqn. 3.2 is applicable if we interpret it as a minimum time that is required for the system to reach the saturation of the magnetic field

$$t_{\rm amp}(E_p) \geq \frac{5}{\Gamma_{\rm NRH}(E_p)}, \tag{3.6}$$

given that the actual maximum energy is E_p. Substituting here the maximum energy of the non-thermal protons that we have found earlier (see sec. 2.6.2), we obtain the time necessary for the amplification close to the maximum possible magnetic field.

Another relevant timescale in our model is the escape time, defined in section 2.6.1. During DSA, the more energy gains a particle, the further it can diffuse away from the shock. Scattering centers for effective scattering are thus important not only in close proximity of the shock. Only 'escaping' CR with the highest energy at a given moment can transfer its energy effectively to the distant turbulence of the corresponding size to support their further growth. Particle acceleration and magnetic field amplification happen simultaneously.

As we discussed earlier, in perpendicular configuration the particle escapes once it advects for the distance r_{g0} away from the shock. It will follow the magnetic field line with no further shock crossing, unable to support further growth of the local magnetic field. We say that escape time $t_{\rm esc\perp}$ (eqn. 2.36) is maximum available for a given particle to amplify the magnetic field before it leaves the shock vicinity.

Hereafter, we will assume

$$t_{\rm amp} = t_{\rm esc\perp}. \tag{3.7}$$

This means that we require instabilities to grow fast enough so that the escaping CR would amplify the magnetic field to the non-linear saturation regime before the escape. This condition is motivated by the fact that for DSA we need a particle to be scattered back to the shock before it advects away by a Larmor radius. Consequently, we need an amplified magnetic field within r_{g0} from the shock. The most moderate condition would hold for the minimum RHS of eqn. 3.2

$$\Gamma_{\rm NRH}(E_{\rm p,max})t_{\rm amp} = 5, \tag{3.8}$$

as this represents that we require minimum sufficient amplification during the available time.

The maximum growth rate can be expressed in terms of the CR energy as

$$\Gamma_{\rm NRH}(E_p) = C_1 \eta_p v_{\rm dr} n_i^{\frac{1}{2}} E_p^{-1}, \tag{3.9}$$

where n_i is ion number density. We assume a diamagnetic drift velocity $v_{\rm dr} = c/5$, and $C_1 = \frac{e\,c}{2}\sqrt{\pi m_i}(\Gamma - 1) = 1.65 \cdot 10^{-11}$ for our sources. We have introduced the acceleration efficiency, that we define as $\eta_p = U_p/U_{\rm kin}$. It happened to be equivalent to

$$\eta_p = \frac{\eta_{\rm p,tot} E_p^{-s+2}}{f_p}, \tag{3.10}$$

where $f_p = E_{\rm p,min}^{-s+2}/(s-2)$. For more detailed calculations see attachments A.2 and A.3. Substituting eqns. 3.9, 2.36 to 3.8 and using eqn. 3.7 we find

$$C_1 \eta_{\rm p} v_{\rm dr} n^{\frac{1}{2}} \frac{1}{E_{p,\rm max\perp}} \frac{E_{p,\rm max\perp}}{ceB_0} = 5. \tag{3.11}$$

Expressing the acceleration efficiency through the eqn. 3.10 we have

$$C_1 \frac{\eta_{\rm p,tot} E_{p,\rm max\perp}^{-s+2}}{f_p} v_{\rm dr} n^{\frac{1}{2}} \frac{1}{ceB_0} = 5. \tag{3.12}$$

We end up with the equation for the non-thermal protons maximum energy in perpendicular magnetic field configuration

$$E_{p,\rm max\perp} = C_2(s) \left[\eta_{\rm p,tot} B_0^{-1} v_{\rm dr} n_i^{\frac{1}{2}} \right]^{\frac{1}{s-2}}, \tag{3.13}$$

where $C_2(s) = \left(\frac{5cef_p}{C_1}\right)^{-\frac{1}{s-2}}$. Now, we are ready to proceed further and calculate the initial magnetic field. Having assumed the equality of $E_{\rm e,max}$ (eqn. 2.20) and $E_{p,\rm max\perp}$ (eqn. 3.13), which was closely discussed in sec. 2.6.2, we find

$$C_2(s) \left[\eta_{\rm p,tot} B_0^{-1} v_{\rm dr} n_i^{\frac{1}{2}} \right]^{\frac{1}{s-2}} = C_e \sqrt{\frac{\nu_c}{B_{\rm eq}}}. \tag{3.14}$$

The equation for the unperturbed magnetic field reads

$$\frac{B_0}{\mu\rm G} = C_B(s) \left(\frac{\nu_c}{10^{14}\rm Hz}\right)^{\frac{-s+2}{2}} \left(\frac{B_{\rm eq}}{100\,\mu\rm G}\right)^{\frac{s-2}{2}} \left(\frac{\eta_{\rm p.tot}}{0.1}\right) \frac{v_{\rm dr}}{c} \left(\frac{n_i}{10^{-4}\,\rm cm^{-3}}\right)^{1/2}, \tag{3.15}$$

where $C_B(s) = C_e^{2-s} C_1/(5cef_p)$. We list the resilting values of B_0 in tab. 3.1.

Table 3.1: From left to right, we list the name of the source and the non-thermal component in the hotspot, the minimum ion number density in the jet n_{min}, the integral number density of the non-thermal protons $U_{\mathrm{p,tot}}$, acceleration efficiency $\eta_{\mathrm{p,tot}}$, the maximum energy of the non-thermal protons $E_{\mathrm{p,max}}$, the unperturbed magnetic field B_0, and the critical magnetic field B_{crit}.

Source	Comp.	n_{min} [cm^{-3}]	$U_{p,\mathrm{tot}}$ [$\mathrm{erg\,cm}^{-3}$]$\cdot 10^{-9}$	$\eta_{\mathrm{p,tot}}$	$E_{\mathrm{p,max}}$ [TeV]	B_0 [μG]	B_{crit} [μG]
3C 105	S1	2.7	3.4	0.38	0.62	0.04	0.00059
	S2	2879	8	0.89	0.19	0.18	0.00092
	S3	2745	7.7	0.86	0.20	0.18	0.00098
3C 227	WS	36	5.1	0.56	0.40	0.079	0.00109
	WN	48	6.2	0.69	0.38	0.099	0.00223
	E	0.29	5.1	0.56	0.90	0.053	0.00168
3C 445	SE	0.55	2.1	0.23	0.81	0.023	0.00079
	SW	1.04	10.5	1.17	0.73	0.12	0.00431

For the comprehensive picture, we briefly summarize here the key steps that led to these results. Based on the observed synchrotron fluxes, we have estimated the equipartition magnetic field, which enabled us to calculate the maximum energy of electrons given that we know the cutoff frequency of the synchrotron spectrum. Looking for a process that would stop the acceleration of the electrons, we have discovered that synchrotron cooling is not the reason. Taking into account perpendicular configuration of the magnetic field, we have assumed that the magnetization downstream is responsible for the particle escape and, consequently, for the end of the acceleration. The magnetization puts the same limitations on escape time of both protons and electrons. Thus we conclude that the maximum achievable energy of protons is the same as for the electrons. To ensure reaching the estimated amplification, we require the growth of the magnetic field (due to the given CR propagation) to be fast enough to reach saturation of the non-linear regime before a CR escapes due to the magnetization. Putting these constraints together allowed us to estimate the unperturbed magnetic field.

According to the numerical simulations [Casse and Marcowith, 2005] the initial value of the magnetic field in the hotspots of the AGNs is orders of magnitude lower than the magnetic field in the hotspot. In tabs. 2.4 and 3.1, we see the values obtained in our calculations. Comparing B_0 and B_{eq} values, we see expected amplification that hints us to the plausibility of our approach.

3.3 Critical magnetic field

The current section is devoted to the discussion of the correctness of the perpendicular configuration assumption.

The configuration of the magnetic field with respect to the shock normal depends on the shock velocity, as we have discussed in sec. 1.5. Another factor that has to be taken into account is the magnetization, as it defines the way how particles behave downstream of the shock. The two possible regimes are

separated by the value of a so-called critical magnetic field $B_{\rm crit}$ [Bell et al., 2018] that is given by the condition

$$l_{\rm min} = r_{\rm g}(B_{\rm crit}) = \frac{E_{\rm p,max\perp}(B_{\rm crit})}{qB_{\rm crit}} = \frac{C_2(s)\left[\eta_{\rm p,tot}B_{\rm crit}^{-1}v_{\rm dr}n_i\right]^{\frac{1}{s-2}}}{qB_{\rm crit}}. \tag{3.16}$$

where $\eta_{\rm p,tot} = U_{\rm p,tot}/U_{\rm kin}$. We calculate these values and list them in the tab. 3.1, based on formula

$$B_{\rm crit} = C_{\rm crit}(s) l_{\rm min}^{-\frac{s-2}{s-1}} \left[\eta_{\rm p,tot}v_{\rm dr}n_i\right]^{-\frac{1}{s-1}}, \tag{3.17}$$

where $C_{\rm crit}(s) = C_2^{-\frac{s-2}{s-1}}(s)$.

In case of the *low magnetization* $B_0 < B_{\rm crit}$, a particle will not gyrate around the magnetic field lines even in case of the perpendicular magnetic field configuration because the spiral trajectory will not fit the size of the system. Effectively, a particle would behave as if it is in a parallel magnetic field.

From tab. 3.1 we can see that for our sample of the hotspots *high magnetization* $B_0 > B_{\rm crit}$ is the case. Therefore the particles will feel the perpendicular magnetic field downstream of the RS of the hotspot. This information was crucial for estimating the magnetic field amplification time as it determines the escape time. In case of the parallel configuration, the escape would most likely occur upstream, leading to the different escape conditions that affect magnetic field amplification and CR acceleration.

We see that this is consistent with our treatment for the magnetic field as being in perpendicular configuration.

Conclusion

In this thesis we have applied a model of the diffusive shock acceleration accompanied with a magnetic field amplification provided by the non-resonant hybrid instabilities on a sample of radiogalaxies. We consider for our study the well observed sources 3C 105, 3C 227 and 3C 445. High resolution data at radio frequencies show the presence of sub-structures (knots) in the hotspots of these sources. We selected 8 knots for our study. Calculations were performed for each knot separately. Based on the evidence, that the observed spectrum of CR is power-law, we study the DSA as a possible mechanism of acceleration.

From the observed synchrotron flux we calculate the allowed range for the magnetic field in knots. Assumed equipartition between the non-thermal protons and electrons with a magnetic field provides the resulting values of B_{eq} field to be of the order of 100μG. We compare these values with the results of numerical simulations [Casse and Marcowith, 2005] and conclude, that B_{eq} is orders of magnitude higher than the expected values, which implies strong amplification of the jet's magnetic field in the hotspot. In the sake of explaining such an amplification, we assume the NRH instabilities as they have the highest growth rate, that is strongly favorable.

Based on the constrains following from the the plasma physics, we verified that the maximum energy of electrons are not given by a synchrotron cooling [Araudo et al., 2016], since it would imply the unreasonably large plasma number densities in hotspots. We further assumed magnetization downstream of the shock to be an alternative mechanism responsible for the synchrotron emission cutoff. This mechanism acts similarly on both protons and electrons, which implies the same resulting maximum energies for both electrons and protons. Additionally, the restriction for the magnetic field amplification arose to fit the observations. Namely, that the magnetic field has to be amplified by a given particle before it advects one Larmor radius from the shock and escapes. To satisfy the latter, we have used a result from the numerical simulations [Bell et al., 2013] that estimate a minimum time required for the magnetic field to grow up to the saturation values.

A consistency of B_0 estimated from the model and numerical simulations [Casse and Marcowith, 2005] indicates that our assumption regarding the magnetization downstream being the main way of CR escape may be correct. By calculating a critical value of the magnetic field, we obtain the confirmation of the high magnetization of the system, which indicates the consistency in assuming magnetic field to be perpendicular to the shock normal.

According to our results the hotspots of the AGNs can not accelerate particles to the UHECR energies through the diffusive shock acceleration. The maximum achievable energy for the selected source is slightly below 1 TeV.

Bibliography

Alexander Aab, Pedro Abreu, Marco Aglietta, Imen Al Samarai, IFM Albuquerque, Ingomar Allekotte, Alejandro Almela, J Alvarez Castillo, Jaime Alvarez-Muñiz, Gioacchino Alex Anastasi, et al. Observation of a large-scale anisotropy in the arrival directions of cosmic rays above 8× 1018 ev. *Science*, 357(6357):1266–1270, 2017.

RUea Abbasi, M Abe, T Abu-Zayyad, M Allen, R Anderson, R Azuma, E Barcikowski, JW Belz, DR Bergman, SA Blake, et al. Indications of intermediate-scale anisotropy of cosmic rays with energy greater than 57 eev in the northern sky measured with the surface detector of the telescope array experiment. *The Astrophysical Journal Letters*, 790(2):L21, 2014.

Anabella T Araudo, Anthony R Bell, Aidan Crilly, and Katherine M Blundell. Evidence that the maximum electron energy in hotspots of fr ii galaxies is not determined by synchrotron cooling. *Monthly Notices of the Royal Astronomical Society*, 460(4):3554–3562, 2016.

Anabella T Araudo, Anthony R Bell, Katherine M Blundell, and James H Matthews. On the maximum energy of non-thermal particles in the primary hotspot of cygnus a. *Monthly Notices of the Royal Astronomical Society*, 473 (3):3500–3506, 2018.

B Arbutina, D Urošević, MM Andjelić, MZ Pavlović, and B Vukotić. Modified equipartition calculation for supernova remnants. *The Astrophysical Journal*, 746(1):79, 2012.

Rainer Beck and Marita Krause. Revised equipartition and minimum energy formula for magnetic field strength estimates from radio synchrotron observations. *Astronomische Nachrichten: Astronomical Notes*, 326(6):414–427, 2005.

AR Bell. The acceleration of cosmic rays in shock fronts–i. *Monthly Notices of the Royal Astronomical Society*, 182(2):147–156, 1978.

AR Bell. Turbulent amplification of magnetic field and diffusive shock acceleration of cosmic rays. *Monthly Notices of the Royal Astronomical Society*, 353(2):550–558, 2004.

AR Bell, KM Schure, B Reville, and G Giacinti. Cosmic-ray acceleration and escape from supernova remnants. *Monthly Notices of the Royal Astronomical Society*, 431(1):415–429, 2013.

AR Bell, AT Araudo, JH Matthews, and KM Blundell. Cosmic-ray acceleration by relativistic shocks: limits and estimates. *Monthly Notices of the Royal Astronomical Society*, 473(2):2364–2371, 2018.

Roger Blandford and David Eichler. Particle acceleration at astrophysical shocks: A theory of cosmic ray origin. *Physics Reports*, 154(1):1–75, 1987.

Roger D Blandford and James P Ostriker. Particle acceleration by astrophysical shocks. *The Astrophysical Journal*, 221:L29–L32, 1978.

Alan H Bridle, David H Hough, Colin J Lonsdale, Jack O Burns, and Robert A Laing. Deep vla imaging of twelve extended 3cr quasars. *The Astronomical Journal*, 108:766–820, 1994.

Georgy I Burde. Particle dynamics and gzk limit in relativity with a preferred frame. *Astroparticle Physics*, 126:102526, 2021.

Fabien Casse and Alexandre Marcowith. Astroparticle yield and transport from extragalactic jet terminal shocks. *Astroparticle Physics*, 23(1):31–56, 2005.

CI Cox, SF Gull, and PAG Scheuer. Three-dimensional simulations of the jets of extragalactic radio sources. *Monthly Notices of the Royal Astronomical Society*, 252(4):558–585, 1991.

RL Diehl. Particle acceleration in cosmic sites. *The European Physical Journal D*, 55(2):509–518, 2009.

JW Dreher, CL Carilli, and RA Perley. The faraday rotation of cygnus a-magnetic fields in cluster gas. *The Astrophysical Journal*, 316:611–625, 1987.

Bernard L Fanaroff and Julia M Riley. The morphology of extragalactic radio sources of high and low luminosity. *Monthly Notices of the Royal Astronomical Society*, 167(1):31P–36P, 1974.

Thomas K Gaisser, Ralph Engel, and Elisa Resconi. *Cosmic rays and particle physics*. Cambridge University Press, 2016.

Graciela B Gelmini. High energy cosmic rays. In *Journal of Physics: Conference Series*, volume 171, page 012012. IOP Publishing, 2009.

Anthony M Hillas. The origin of ultra-high-energy cosmic rays. *Annual review of astronomy and astrophysics*, 22:425–444, 1984.

Jörg R Hörandel. Cosmic rays from the knee to the second knee: 1014 to 1018ev. *Modern Physics Letters A*, 22(21):1533–1551, 2007.

JG Kirk, AW Guthmann, YA Gallant, and A Achterberg. Particle acceleration at ultrarelativistic shocks: an eigenfunction method. *The Astrophysical Journal*, 542(1):235, 2000.

John G Kirk, David Blair Melrose, and Eric Ronald Priest. *Plasma Astrophysics: Saas-Fee Advanced Course 24. Lecture Notes 1994. Swiss Society for Astrophysics and Astronomy*, volume 24. Springer Science & Business Media, 2006.

GF Krymskii. A regular mechanism for the acceleration of charged particles on the front of a shock wave. In *Akademiia Nauk SSSR Doklady*, volume 234, pages 1306–1308, 1977.

Kenneth R Lang. *Astrophysical Formulae: Space, time, matter and cosmology*. Springer, 2013.

JP Leahy, ARS Black, J Dennett-Thorpe, MJ Hardcastle, S Komissarov, RA Perley, JM Riley, and PAG Scheuer. A study of fr ii radio galaxies with z¡ 0.15—ii. high-resolution maps of 11 sources at 3.6 cm. *Monthly Notices of the Royal Astronomical Society*, 291(1):20–53, 1997.

EM Lifshitz and LD Landau. Fluid mechanics: Volume 6 (course of theoretical physics), 1987.

Malcolm S Longair. *High energy astrophysics*. Cambridge university press, 2010.

K-H Mack, MA Prieto, G Brunetti, and M Orienti. Near-infrared/optical counterparts of hotspots in radio galaxies. *Monthly Notices of the Royal Astronomical Society*, 392(2):705–717, 2009.

Silvano Massaglia. Constraining the parameters of agn jets. In *Jets in Young Stellar Objects*, pages 223–233. Springer, 2003.

James H Matthews, Anthony R Bell, Katherine M Blundell, and Anabella T Araudo. Fornax a, centaurus a, and other radio galaxies as sources of ultrahigh energy cosmic rays. *Monthly Notices of the Royal Astronomical Society: Letters*, 479(1):L76–L80, 2018.

K Meisenheimer and AF Heavens. Particle acceleration in the hotspot of the jet of quasar 3c273. *Nature*, 323(6087):419–422, 1986.

M Orienti, MA Prieto, G Brunetti, K-H Mack, Francesco Massaro, and DE Harris. Complex particle acceleration processes in the hotspots of 3c 105 and 3c 445. *Monthly Notices of the Royal Astronomical Society*, 419(3):2338–2348, 2012.

M Orienti, G Migliori, G Brunetti, H Nagai, F D'Ammando, KH Mack, and MA Prieto. Jansky vla observations of synchrotron emitting optical hotspots of 3c 227 and 3c 445 radio galaxies. *Monthly Notices of the Royal Astronomical Society*, 494(2):2244–2253, 2020.

RA Perley, AG Willis, and JS Scott. The structure of the radio jets in 3c449. *Nature*, 281(5731):437–442, 1979.

Michael D Smith, Michael L Norman, Karl-Heinz A Winkler, and Larry Smarr. Hotspots in radio galaxies: a comparison with hydrodynamic simulations. *Monthly Notices of the Royal Astronomical Society*, 214(2):67–85, 1985.

Georgi T Zatsepin and Vadem A Kuz'min. Upper limit of the spectrum of cosmic rays. *Soviet Journal of Experimental and Theoretical Physics Letters*, 4:78, 1966.

List of Figures

List of Tables

Appendix A

Attachments

A.1 Abbreviations

CR - cosmic rays
UHECR -Ultra-high energy cosmic rays
AGN - Active Galactic Nuclei
FR - Fanaroff–Riley classification
GZK limit - Greisen–Zatsepin–Kuzmin limit
DSA - Diffusive shock acceleration
RS - reverse shock
BS - bow shock
CD - contact discontinuity
SNR - Supernova remnant
IGM - intergalactic medium
dHT frame - de Hoffmann/Teller reference frame
RHS - right-hand side
VLA - Very Large Array
VLT - Very Large Telescope
NRH instabilities - non-resonant hybrid instabilities (also called Bell instabilities)
MHD - Magnetohydrodynamics

A.2 Acceleration efficiency

We define the acceleration efficiency of protons in terms of the proton energy density U_p as

$$\eta_p = \frac{U_p}{U_{\mathrm{kin}}} \tag{A.1}$$

and the total proton acceleration efficiency as

$$\eta_{\mathrm{p,tot}} = \frac{U_{\mathrm{p,tot}}}{U_{\mathrm{kin}}}, \tag{A.2}$$

where $U_{\mathrm{p,tot}} = \int U_p/EdE$ is an integral energy density of non-themal protons. Combining the above equations and using $U_p = N(E_p)E_p^2 \equiv K_p E_p^{-s+2}$ and

$U_{\mathrm{p,tot}} = K_p f_p$ we find

$$\eta_p = \frac{U_p}{U_{\mathrm{p,tot}}}\eta_{\mathrm{p,tot}} = \frac{K_p E_p^{-s+2}}{K_p f_p}\eta_{\mathrm{p,tot}} = \frac{E_p^{-s+2}}{f_p}\eta_{\mathrm{p,tot}}, \tag{A.3}$$

where K_p is a normalization function of the non-thermal proton spectrum, and $f_p = E_{\mathrm{p,min}}^{-s+2}/(s-2)$ with $E_{\mathrm{p,min}} = 50 m_p c^2$. Substituting $\eta_{\mathrm{p,tot}}$ from the eqn. A.2 we find

$$\eta_p = \frac{U_{\mathrm{p,tot}} E_p^{-s+2}}{\mathrm{f_p U_{kin}}}. \tag{A.4}$$

We can calculate the energy density of the non-thermal protons $U_{\mathrm{p,tot}}$ substituting $U_{\mathrm{e,tot}}$ from eqn. 2.15 to eqn. 2.13, giving

$$U_{\mathrm{p,tot}} = \frac{a}{(1+a)}\frac{B_{\mathrm{eq}}^2}{8\pi}. \tag{A.5}$$

Substituting this to eqn. A.2 we can determine the acceleration efficiency. We list values of $U_{\mathrm{p,tot}}$ and $\eta_{\mathrm{p,tot}}$ in tab. 3.1.

A.3 Maximum NRH-growth rate in terms of acceleration efficiency

In the following paragraph we will express the maximum growth rate in form that will bring us closer to the maximum energy determination. We start from the eqn. 3.1, that is equivalent to

$$\Gamma_{\mathrm{NRH}} = \frac{1}{2}\frac{j_{\mathrm{CR}}}{c}\sqrt{\frac{\pi}{m_p\, n_i}} = \frac{e v_{\mathrm{dr}}}{2c}\sqrt{\frac{\pi}{m_p\, n_i}} n_{\mathrm{CR}} \tag{A.6}$$

The number density of the particles of a given energy is given by

$$n_{\mathrm{CR}} = K_p E_p^{-s+1} = \frac{U_{\mathrm{p,tot}}}{f_p} E_p^{-s+1} \tag{A.7}$$

Expressing from the eqn. A.4

$$U_{\mathrm{p,tot}} = \frac{\eta_p f_p}{E_p^{-s+2}} U_{\mathrm{kin}} \tag{A.8}$$

we find the non-thermal number density of protons

$$n_{\mathrm{CR}} = \frac{\eta_p f_p E_p^{-s+1}}{f_p E_p^{-s+2}} U_{\mathrm{kin}} = \eta_p U_{\mathrm{kin}} E_p^{-1}. \tag{A.9}$$

The resulting maximum growth rate

$$\Gamma_{\mathrm{NRH}} = \frac{e v_{\mathrm{dr}}}{2c}\sqrt{\frac{\pi}{m_p n_i}}\eta_p E_p^{-1} U_{\mathrm{kin}} = \frac{e v_{\mathrm{dr}}}{2c}\sqrt{\frac{\pi n_i}{m_p}}\eta_p E_p^{-1}(\gamma-1) m_i c^2 \tag{A.10}$$

We introduce a numerical factor $C_1 = \frac{e\,c}{2}\sqrt{\pi m_i}(\gamma-1) = 1.65 \cdot 10^{-11}$, so we can write

$$\Gamma_{\mathrm{NRH}} = C_1 \eta_p v_{\mathrm{dr}} n_i^{\frac{1}{2}} E_p^{-1}. \tag{A.11}$$

Note, that the maximum growth rate depends on the energy of the CR that drive the growth of the instabilities.